SEDIMENTATION, SEDIMENT STRENGTH, AND ORIGIN OF TUAHENI LANDSLIDE COMPLEX, HIKURANGI MARGIN, OFFSHORE NORTH ISLAND NEW ZEALAND

by

Travis Vick

A thesis submitted to the Faculty and the Board of Trustees of the Colorado School of Mines in partial fulfillment of the requirements for the degree of Master of Science (Geophysics).

Golden, Colorado

Date ___________________________

Signed: ________________________

Travis J. Vick

Signed: ________________________

Dr. Brandon Dugan

Thesis Advisor

Golden, Colorado

Date ___________________________

Signed: ________________________

Dr. Paul Sava

Professor and Department Head

Department of Geophysics

ABSTRACT

We investigate the origin of the Tuaheni Landslide Complex (TLC) by high sedimentation rates and fluid flow at deposition using core sample and log data from International Ocean Discovery Program (IODP) Expedition 372 Site U1517. Understanding how submarine landslides develop failure zones and weaken with time is important for identifying the potential for future failure that can impact infrastructure, generate tsunamis, and affect human life. In this study we construct a 1-D sedimentation-fluid flow model to simulate the pressure evolution within the sedimentary column through time. We focus on pressures in previously identified zones of weakness to investigate if overpressure (pressure over hydrostatic) was sufficiently high to cause failure. Our analysis includes comparing the overpressure to the onset of failure estimated with an infinite slope factor of safety approach. To better understand sediment properties after failure we run direct simple shear (DSS) tests on five core samples at different depths in and below the TLC. Based on our integrated modeling and experimental approach, we find that the high sedimentation rates during the deposition of the sediments at the failure zone produced enough overpressure to cause failure. Our DSS experiments constrain strain weakening and pore pressure generation within these sediments during failure. When we put this together, we define a way for a homogeneous system to fail at deposition, weaken with failure and strain, and experience creeping deformation.

CONTENTS

LIST OF FIGURES

LIST OF TABLES

LIST OF EQUATIONS

ACKNOWLEDGEMENTS

I would like to first and foremost express my most sincere gratitude and appreciation to my advisor Dr. Brandon Dugan for his constant support, encouragement, understanding, and flexibility during this research and thesis undertaking. Dr. Dugan's mentorship during this master's research project greatly surpassed any necessary obligation and exhibited the character of a caring advisor. Without his insight, mentoring, and patience this work would not have come to fruition.

I would also like to thank the International Ocean Discovery Program and the National Science Foundation for providing the funding and data necessary to complete this research. I also thank the Colorado School of Mines Department of Geophysics for their financial support and making the graduate process as easy and smooth as possible.

Lastly, I would like to thank my family and friends for their faithful support of my endeavors and loving encouragement to challenge myself.

CHAPTER 1

INTRODUCTION TO SLOPE STABILITY AND THE TUAHENI LANDSLIDE COMPLEX

Large submarine landslides may occur less frequently than other natural disasters, such as earthquakes, however they can produce similar or worse outcomes (Solheim et al., 2005; Harbitz et al., 2013). Submarine landslides can be destructive by generating damaging tsunamis that have both onshore and offshore impacts to infrastructure and life (Bardet et al., 2003; Talling et al., 2014). The destructive nature is due in part to the volumetric extent of the submarine landslides, which can occur in sizes up to thousands of cubic kilometers, larger on average than terrestrial landslides (Hampton et al., 1996). With slope failures occurring on both passive and active margins, the environments for these hazards are vast and allow for widespread impacts on people and nature.

Submarine landslides can have negative impacts to offshore infrastructure causing detriment to humans and the environment. The 1929 Grand Banks submarine landslide provides a modern example of submarine slides damaging marine infrastructure. The sediment mobilized in this failure broke 12 transatlantic telegraph cables, causing international communication issues (Heezen and Drake, 1964). In addition, structures routinely built in these environments to drill and acquire fossil fuel resources can be in danger of submarine slope failure. One such occurrence happened in 2004 in which a Taylor Energy Company platform on the continental shelf in the Gulf of Mexico was toppled by a hurricane-induced submarine landslide (Bryant et al., 2020). The resultant long-lasting oil spill has caused long-term pollution of the Gulf of Mexico (Sun et al., 2018). Such incidents provide reason to further understand how and under what conditions these slope failures occur.

While these natural phenomena have offshore implications, their effects also reach onshore. Apart from damage from direct interaction, the large volume of sediment moved in submarine landslides can generate tsunamis (e.g., Talling et al., 2014). Within the last century, large submarine landslides have initiated tsunamis offshore Aitape, Papua New Guinea (Bardet et al., 2003; Tappin et al., 2008), Flores Island, Indonesia (Imamura et al., 1995), and Grand Banks, Newfoundland (Fine et al., 2005; Schulten et al., 2018). Tsunamis from these three submarine landslides have caused thousands of human deaths (Imamura et al., 1995; Bardet et al., 2003; Fine et al., 2005). In addition, these tsunamis destroyed coastal cities (Imamura et al., 1995; Bardet et al., 2003; Fine et al., 2005). In each case, a lack of tsunami alert warnings failed to let the city residents know of the ensuing danger. Further insight on the causes of the slope instability that initiated these tsunamis can be used to help with improving risk assessment and early warning.

Societal impacts of submarine landslides have motivated previous studies to investigate submarine landslide formation and evolution to mitigate their associated disasters. This includes estimating external forces that can trigger landslides, such as earthquakes (Chugh and Thun, 1985; Biscontin et al., 2003; Biondi et al., 2007). Mountjoy et al. (2018) document that on active margins, earthquakes are a primary tectonic driver of mass sediment deposits from continental shelves to deepwater basins. However, earthquakes are not the only factor causing slope failures, so there is still uncertainty in understanding the initiation factors of such large sediment movements. With submarine landslides being a primary conduit of this transportation of large sediment volumes across both marine shelf and slope environments, understanding their formation and development may help assess failure initiation (Masson et al., 2006).

Research in failure initiation of submarine landslides involving the movement of large quantities of sediment remains active and incorporates studies on pore pressure drive. Occurring on continental slopes dipping from less than one degree to tens of degrees, one reason for these mass waste events' failures is overpressure generation (Gibson, 1958; Hubbert and Rubey, 1959; Bredehoeft and Hanshaw, 1968; Koppula and Morgenstern, 1982; Bethke 1986; Urlaub et al., 2015). Overpressure is pore pressure in excess of hydrostatic conditions. The source of the overpressure required for slope failure varies across the globe, with certain overpressure-generating mechanisms better understood than others. One commonly understood cause for high overpressure generation is rapid sedimentation of low permeability materials (Dugan and Stigall, 2010; Green and Wang, 1986; Gibson, 1958). Pore pressure in this case increases due to the compaction of saturated sediments whose pore fluid does not escape during deposition. Lithologic factors can also have an impact on pore pressure and slope failure. An example of a lithologic control comes from studies on diatomaceous ooze layers. Previous work on diatomaceous ooze hypothesize that diatom rich layers are culpable for failures on continental margins globally (Urlaub et al., 2018). This is in part due to the ability of diatoms to retain large quantities of water taking longer for this lithology to dewater and resulting in overpressure. A second cause for overpressure and slope instability is the presence of gas hydrates. Gas hydrate destabilization releases free gas generally into shallower sediments, driving up pore pressures (McIver, 1982). The release of methane from the gas hydrate zone that typically accompany sediments in continental shelf and slope environments is also a potential climatic hazard (Nisbet et al., 1998; Maslin et al., 2004; Talling et al., 2014).

Other studies tackle the slope instability phenomena by investigating failure due to weak layers caused by mineralogic variation (Nakamura et al., 2010; Couvin et al., 2020).

The presence of heterogeneity in mineralogy can lead to distinct interfaces accommodating strain. The strength properties that can exist at these interfaces allow for the creation of zones of weakness. One example is the presence of zeolites in sediments has been shown to alter the rheology of the host sediment (Miramontes et al., 2018). Zeolites promote strain softening, so with sufficient strain, shear strength decreases enough to allow for rapid failure. The low shear strength zones now constitute inherited weak layers.

Understanding how failure occurs, at locations where lithologic factors do not vary and where there is not an influx of disassociated gas, leads to our study of the Tuaheni Landslide Complex (TLC). Submarine landslide behavior and specifically failure initiation in a homogeneous system is a more poorly understood environment in the field of slope instability and failure. Our work focuses to further the research on the question of slope failure in homogeneous lithologies.

Our research builds on previous studies by looking at failure-initiating processes and the resulting changes in sediment strength. We provide new insight into the behaviors of submarine landslides that can be applied to other similar environments such as the Norwegian continental margin (Haflidason et al., 2003; L'Heureux et al., 2011). We focus on the TLC which is interpreted to be actively creeping on a homogeneous shear zone (Mountjoy et al., 2014). We integrate sedimentation and fluid pressure buildup for this margin through sedimentation-fluid flow models to identify the conditions where failure was likely. We base these models on measured permeability, storativity, and sedimentation rates estimated from logging and core data. We then discuss failure evolution based on results of direct simple shear experiments. With this integrated approach we identify how sedimentation-initiated slope failure leads to strain weakening in the shear zone, ultimately creating a permanent zone of weakness.

The TLC located offshore the east coast of the North Island of New Zealand (Figure 1.1), is made up of two distinct deposits (Figure 1.1C) (Gross et al., 2018); TLC1 is the upper, actively deforming layer and is underlain by TLC2 (Mountjoy et al., 2014; Gross et al., 2018; Couvin et al., 2020). TLC2 is interpreted to be a deposit that is not actively deforming (Gross et al., 2018). Mountjoy et al. (2014) and Pecher et al. (2018) propose that failure of the TLC could be influenced by gas hydrate dissociation or deeper-sourced fluid influx into the basin. These studies were informed by bathymetric and seismic data interpretations of the TLC geometry and deformation structures.

IODP Expedition 372 drilled, logged, and cored through the TLC (Barnes et al., 2019) which provided first-order tests for the influence of gas hydrates on the slide complex. Petrophysical interpretations and geochemical data show that the top of gas hydrate occurrence is ~100 mbsf (meters below sea floor) whereas the base of TLC1 is 37 mbsf and the base of TLC2 is 67 mbsf (Barnes et al., 2019; Screaton et al., 2019). Migration of free gas from hydrate dissociation is unlikely to reach the active portion of the TLC1 (Screaton et al, 2019). Based on these results, we evaluated the role of sedimentation and vertical fluid flow on the initiation of failure, and how strain softening during failure created an induced weak zone in a homogeneous sedimentary section. This induced weak layer now accommodates the creeping manner of the submarine landslide (Mountjoy et al., 2009). We investigate this through integration of physical property data, geotechnical laboratory experiments, and numerical models. Data from and research following IODP Expedition 372 shows that gas and gas hydrates are not likely involved in the TLC failure. As such, we look at other mechanisms for initial failure and the observed weakness. Our work advances the study of the TLC through the integration of physical property data and sedimentation rates to investigate the onset of failure of TLC1.

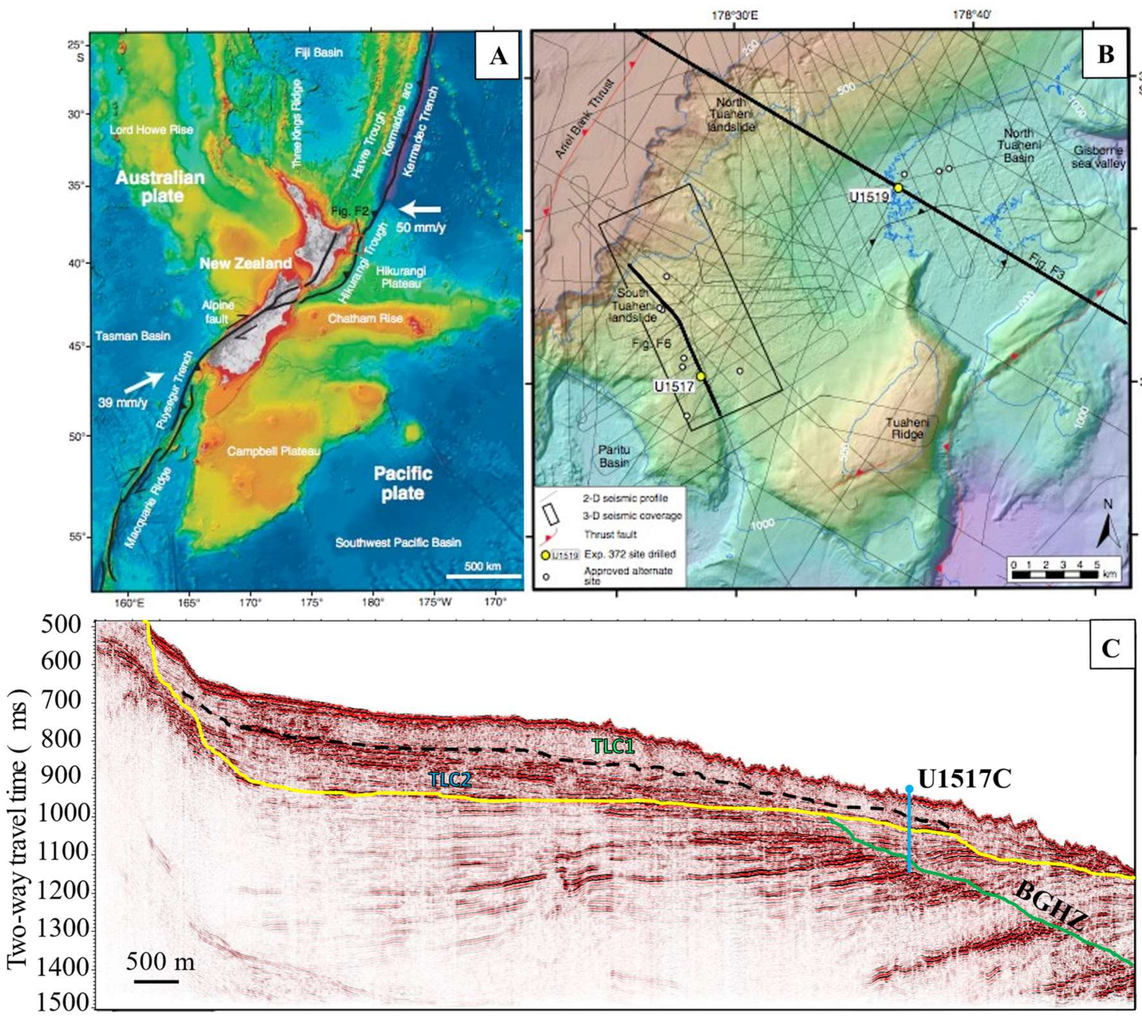

Figure 1.1: A) Topography and bathymetry map of New Zealand, showing the location of the Tuaheni Landslide Complex (TLC). B) Location of seismic lines and seismic surveys over the TLC and the IODP Expedition 372 Site U1517. C) Two-way travel time seismic section with interpreted horizons of interest including TLC1 and TLC2. The yellow line denotes the base of the landslide debris, and the green line denotes the base of the gas hydrate stability zone (Barnes et al., 2019).

CHAPTER 2

METHODS AND MATERIALS

2.1 Methodology Description

In this research we utilize numerical approaches coupled with experiments to surmise the failure evolution of the TLC. In the following sections we will describe the methodology used in DSS experiments, the expected data outcome of the DSS experiments, and the principles the DSS experiments are based on. Additionally, we will describe the type of numerical modeling used and its necessary inputs.

2.2 Direct Simple Shear Experiments

We ran direct simple shear (DSS) experiments on five samples collected at International Ocean Discovery Program (IODP) Expedition 372 Site U1517. These 5 samples are from 38.84, 72.26, 79.73, 117.21, and 181.09 mbsf include sediment from within and below the interpreted base of the Tuaheni Landslide Complex (TLC) (Mountjoy et al., 2014; Barnes et al., 2019). After initial multi-sensor core logging in the original, plastic core liner, samples were sealed in their core liners and stored at 4°C, to maintain in situ water content and to minimize microbial activity. Samples were then shipped in refrigerated containers and stored in a laboratory refrigerator prior to DSS experiments. Samples were only removed from the sealed liners when being prepared for experiments. During preparation for experiments, visual inspection was used to confirm the samples had no indicators of sample disturbance such as mud clasts or stress fractures (Kubo et al., 2020).

2.2.1 Sample Preparation

Each DSS experiment began with sample preparation. This involved trimming the sample into a right cylinder. The shallowest four samples were trimmed to right cylinders of 66.29 mm (diameter) by 18.57 mm (height). The deepest sample was trimmed to a right cylinder of 50.80 mm (diameter) by 18.80 mm (height) to allow loading to a higher normal stress representative of the sample's burial depth. The diameter and height of each sample is used to calculate the total volume (V_t). Trimmings taken from the core samples are weighed while saturated, placed in an oven to dry for at least 72 hours at 38°C, and then reweighed to measure the dry sample mass. We then divide the dry mass by the grain density of 2.7 g/cm^3, determined from Expedition 372 measurements, to determine the sample's total volume of solids (V_s) (Barnes et al., 2019). The volume of solids is used to calculate the initial void ratio (e) of the sample,

$$e = (V_t - V_s)/V_s. \quad (2.1)$$

Each trimmed sample is placed between two porous discs, enclosed in a flexible rubber membrane, and confined by metal rings to provide structure and to distribute the shear force across the sample as per the DSS standard (ASTM International, 2007). Once placed into the DSS apparatus the sample is connected to a pipette of water which is monitored to ensure the sample remains saturated throughout the experiment.

2.2.2 Consolidation Phase

The consolidation stage uses incremental loading to load each sample to its pre-consolidation stress, which we assume is consistent with the vertical effective stress for hydrostatic conditions. We assume hydrostatic conditions due to our pressure data point that shows current hydrostatic pressure. In this stage, the normal load is increased in steps up to the in situ vertical effective stress (Figure 2.1). Each step involves a rapid increase in normal load that is maintained while pore pressure dissipates; once pressure has dissipated, the next load increment is applied (Figure 2.1). Dissipation is confirmed by monitoring sample height; height stops changing after pressure has been fully dissipated. The pressure dissipation duration increases with increasing load due to the decrease in permeability associated with consolidation and porosity loss.

2.2.3 Shear Deformation Phase

After the sample has been loaded to the interpreted pre-consolidation stress, and all the excess pore pressure has dissipated, the shear deformation phase begins. During simple shear deformation, the normal force is adjusted to maintain a constant sample volume. The horizontal force is applied and adjusted to maintain a constant rate of displacement of 0.0051 mm/min. Shear strain (γ) is defined as

$$\gamma = 100\left(\frac{\delta}{h}\right), \tag{2.2}$$

where shear displacement (δ) is the displacement from the beginning of the shear stage and height (h) is the sample at height at the beginning of the shear stage (ASTM International, 2007).

During simple shear deformation we document the normal load changes required to keep the sample at a constant post-consolidation, pre-shear volume (Figure 2.2). Any increase in normal load to keep the sample volume constant is then directly related to the shear induced pore pressure (Δus),

$$\Delta us = \sigma'_{nc} - \sigma'_{n}, \tag{2.3}$$

where σ'_{nc} is maximum pre-shear normal stress, and σ'_{n} is instantaneous normal stress during shear (ASTM International, 2007) (Figure 2.2).

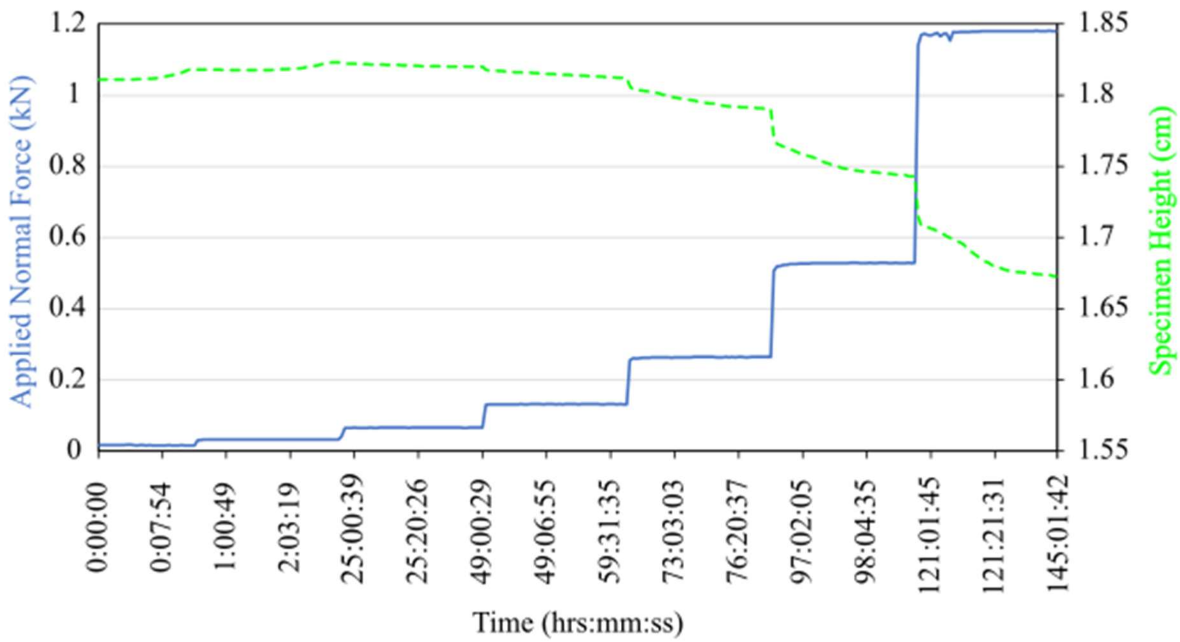

Figure 2.1: Applied normal force (blue) showing the incremental load steps and associate change in sample height (green) during the consolidation stage of the direct simple shear (DSS) experiment on the sample from 38.84 mbsf.

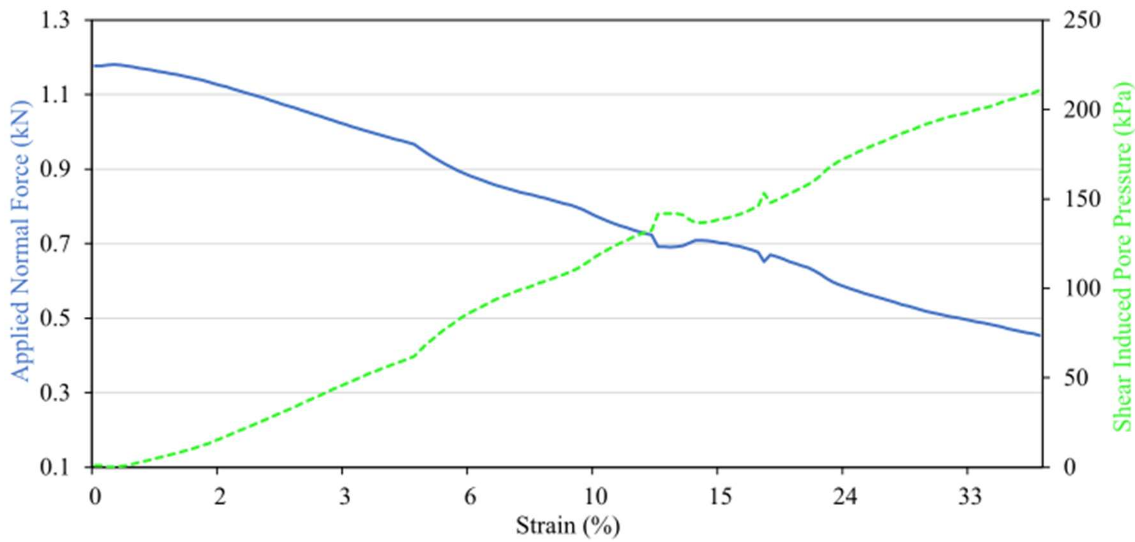

Figure 2.2: Applied normal force (blue) and calculated shear-induced pore pressure (green) [Eq. 2.3] during the shear deformation stage of the DSS experiment for the sample from 38.84 mbsf.

2.3 Sedimentation-Fluid Flow Modeling

In order to examine the role of rapid sedimentation on the development of overpressure within the system, we simulate 107,500 yrs of sedimentation in a 1D finite-difference model. We model this time interval because it is constrained by biostratigraphic and isotope dating methods and accounts for the deposition of 100 m of sediment which extends beyond our focus; the TLC deposit extends from 0-66.6 mbsf.

Our forward model simulates 1-D deposition and consolidation of sediments on a basal, no-flow boundary. At all times the upper boundary is the seafloor, a hydrostatic boundary. Our model solves for overpressure (P*, pressure in excess of hydrostatic) through time (Gibson, 1958),

$$\frac{\partial P^*}{\partial t} = c_v \left(\frac{\partial^2 P^*}{\partial z^2}\right) + \gamma' \frac{\partial h}{\partial t}, \tag{2.4}$$

where c_v is the coefficient of consolidation, γ' is the effective unit weight of the sediments, and $\partial h/\partial t$ is the sedimentation rate. The coefficient of consolidation is calculated based on the dynamic viscosity of water (μ=0.001 Pa*s), the storativity (St), and permeability (k) of the system,

$$c_v = \frac{k}{\mu * St}. \tag{2.5}$$

Previously completed constant rate of strain consolidation experiments provide constraints on the in situ permeabilities for the samples (Dugan et al., 2018). The storativity of the system is calculated using porosity and compressibility values (Dugan and Flemings, 2002),

$$St = \frac{\varphi_0 * \beta}{1-\varphi_0} + \varphi_0 * \beta_f. \tag{2.6}$$

A regression of measured porosity and hydrostatic vertical effective stress from sediments from 0-10 mbsf is used to determine depositional porosity (φ_0) and bulk compressibility (β) (Hubbert and Rubey, 1959; Dugan and Flemings, 2000),

$$\varphi = \varphi_0 * e^{-\beta(S_v - \rho_w g z - P^*)}, \tag{2.7}$$

where S_v is the vertical effective stress, g is the gravitational acceleration, and z is the depth. The regression with R^2=0.75 provides a φ_0 of 0.504 % and a β of 5.68e-6 Pa^{-1} (Figure 2.3).

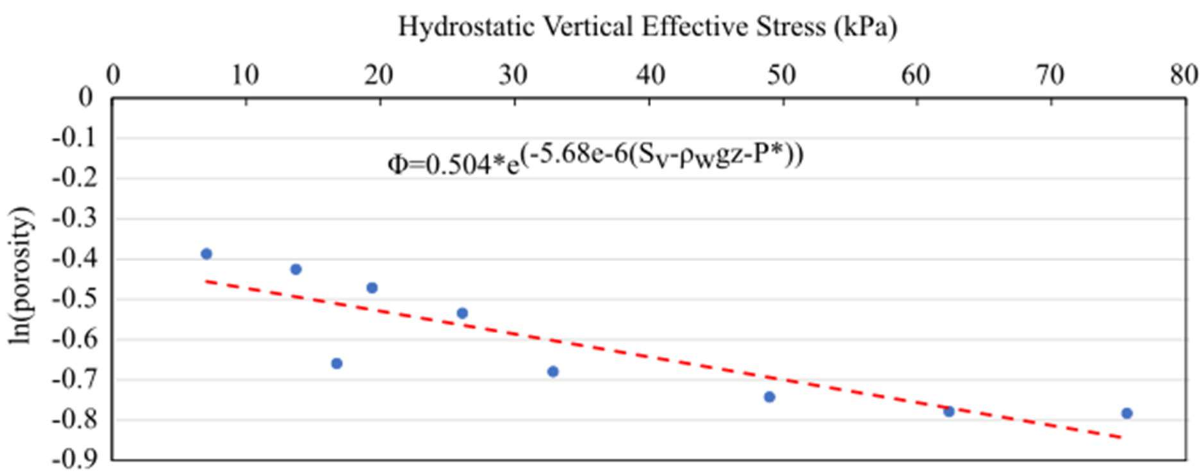

Figure 2.3: Regression of the natural log of porosity against the hydrostatic vertical effective stress at the porosity data points' respective depths (R^2 = 0.752). The regression provides the bulk compressibility beta value for the upper 10 m of landslide deposition.

Using our constrained values of initial porosity and bulk compressibility, a β_f of 5.0e-10 Pa^{-1}, and our estimated in situ permeabilities, we estimate that c_v ranges from 5.2e-9 to 5.8e-7 m^2/s. For simplicity, we present results based on constant coefficient of consolidation of 3.5e-8 m^2/s, and then discuss the implications of lower and higher c_v values.

To calculate the effective unit weight for the modeling, we use the difference between the saturated unit weight (γ_s) and the unit weight of water (γ_w),

$$\gamma' = \gamma_s - \gamma_w = (\rho_b - \rho_w)g \tag{2.8}$$

where the density of water (ρ_w) is 1024 kg/m^3 for seawater and the bulk density (ρ_b) is 1830 kg/m^3 based on core and logging data (Barnes et al., 2019).

The third input to model overpressure is the sedimentation rate. These values result from previous analysis of samples from Site U1517 using biostratigraphic and radiocarbon isotope dating methods (Barnes et al., 2019). Our sedimentation rates range from 0.487 mm/yr to 79.474 mm/yr (Figure 2.4) (Barnes et al., 2019; Couvin et al., 2020).

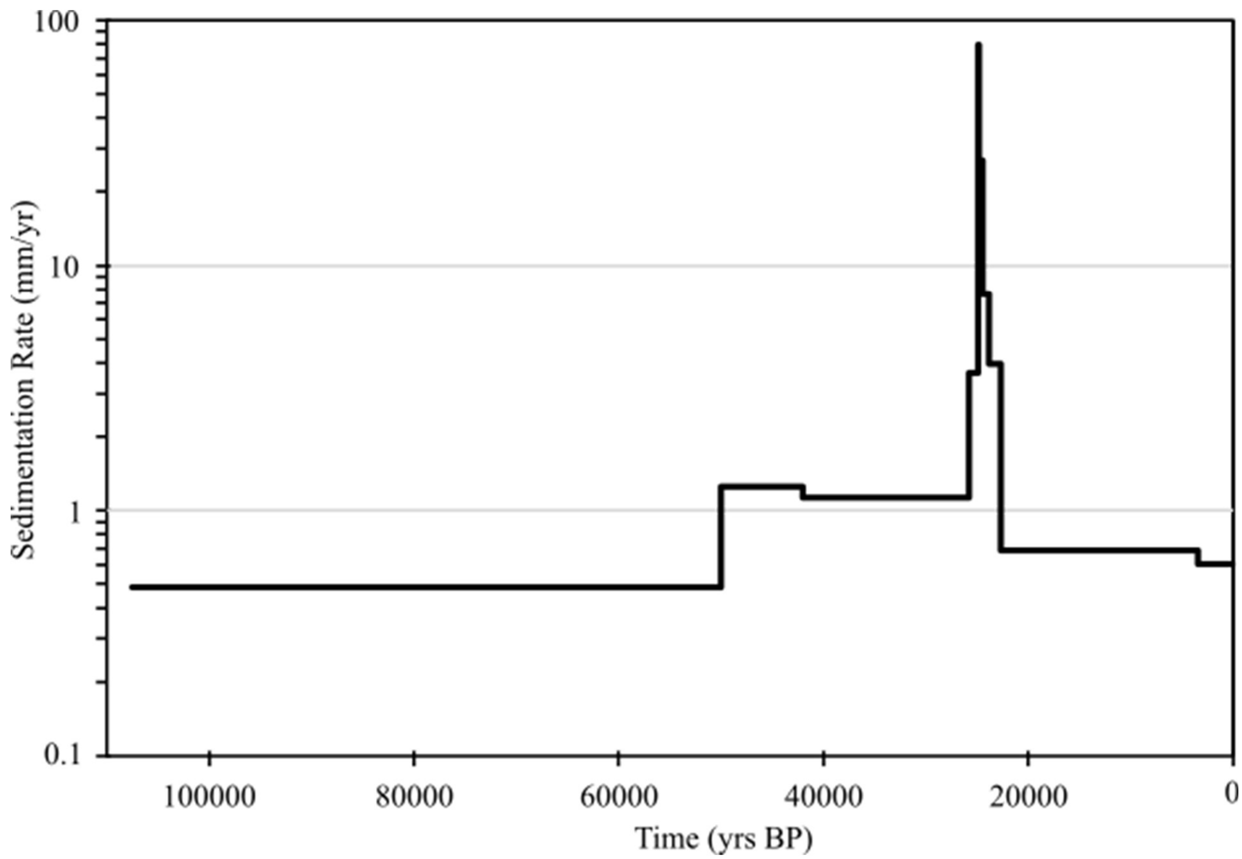

Figure 2.4: The sedimentation rates used for the sedimentation-fluid flow numerical modeling plotted against deposition time in years before present (BP).

With these parameters we are able to predict how fluid pressure evolves in this sedimentary system due to sedimentation and fluid flow. We then relate the overpressure to the potential for the slope failure along discrete stratigraphic horizons during time. We also validate the model against modern, in situ pressure observations. The five horizons of interest are 30 mbsf, 37 mbsf, 38.84 mbsf, 59 mbsf, and 75 mbsf. We examine these intervals in order to connect current interpreted failure locations (weak layer, decollement, base of landslide) with past locations of overpressure with potential of failure. The modeled deeper horizons of interest are used for model validation.

CHAPTER 3

SEDIMENTATION, SEDIMENT STRENGTH, AND ORIGIN OF TUAHENI LANDSLIDE COMPLEX, HIKURANGI MARGIN, OFFSHORE NORTH ISLAND NEW ZEALAND

3.1 Introduction

While large submarine landslides may occur less frequently than other natural disasters, such as earthquakes, they can produce similar or worse outcomes (Solheim et al., 2005; Harbitz et al., 2013). Submarine landslides can be destructive by generating damaging tsunamis that have onshore impacts, causing damage to offshore infrastructure, and releasing methane from gas hydrates (Bardet et al., 2003; Talling et al., 2014). With slope failures occurring on both passive and active margins, the environment for these failures is vast. Continental passive margins are known to be locations of extensive oil and gas accumulations. Structures routinely develop in these environments to drill and acquire the fossil fuel resources, and they can be in danger of slope failure. Apart from major industry, such shallowly dipping slopes where these landslides occur allow for the generation of large tsunamis (e.g., Talling et al., 2014). Within the last century, submarine landslides have initiated tsunamis offshore Papua New Guinea (Bardet et al., 2003; Tappin et al., 2008), Flores Island (Imamura et al., 1995), and Grand Banks (Fine et al., 2005; Schulten et al., 2018) taking thousands of human lives. Another geohazard that these landslide failures can instigate is the release of methane from the gas hydrate zone that typically accompany sediments in continental shelf and slope environments (Nisbet et al., 1998; Maslin et al., 2004; Talling et al., 2014). Due to these geohazards, previous studies have investigated different aspects of submarine landslide formation and evolution to mitigate their associated disasters. This includes estimating external forces that can trigger landslides, such as earthquakes

(Chugh and Thun, 1985; Biscontin et al., 2003; Biondi et al., 2007). Mountjoy et al. (2018) document that on active margins earthquakes are the primary force driving mass sediment deposits from continental shelves to deepwater basins along the continental slope. Given that submarine landslides transport large volumes of sediment across marine shelf and slope environments, it is important to understand their formation and development through time (Masson et al., 2006). Other studies have investigated failure due to weak layers caused by mineralogic variation (Nakamura et al., 2010; Couvin et al., 2020). However, there is still uncertainty in understanding the initiation factors of such large sediment deposit failures.

Our research builds on previous studies by looking at the processes that initiate failure and the associated changes in sediment properties. This provides new insight into the behaviors of submarine landslides that can be applied to several other similar environments (Haflidason et al., 2003; L'Heureux et al., 2011). We focus on the Tuaheni Landslide Complex (TLC) which is interpreted to be actively creeping on a homogeneous shear zone (Mountjoy et al., 2014). We integrate sedimentation and fluid pressure buildup for this margin through sedimentation-fluid flow models to identify the conditions where failure was likely. We base these models on measured permeability, storativity, and sedimentation rates estimated from logging and core data. We then discuss failure evolution based on results of direct simple shear experiments. With this integrated approach we identify how sedimentation-initiated slope failure leads to strain weakening in the shear zone.

3.2 Background

The TLC located offshore the east coast of the North Island of New Zealand (Figure 3.1), is made up of two landslide deposits (Figure 3.1C) (Gross et al., 2018); TLC1 is the upper, actively deforming layer and is underlain by TLC2 (Mountjoy et al., 2014; Gross et al., 2018; Couvin et al., 2020). TLC2 is interpreted to be a failure deposit that is not actively deforming (Gross et al., 2018). Mountjoy et al. (2014) and Pecher et al. (2018) propose that failure of the TLC could be influenced by gas hydrate dissociation or deeper-sourced fluid influx into the basin. These studies were informed by bathymetric and seismic data interpretations of the TLC geometry and deformation structures. Our work advances the study of the TLC through the integration of physical property data and sedimentation rates to investigate the onset of failure of TLC1.

IODP Expedition 372 drilled, logged, and cored through the TLC (Barnes et al., 2019), which provided first-order tests for the influence of gas hydrates on the slide complex. Petrophysical interpretations and geochemical data showed that the top of gas hydrate occurrence was ~100 mbsf (meters below sea floor) whereas the base of TLC1 is 37 mbsf and the base of TLC2 is 66.6 mbsf (Barnes et al., 2019, Screaton et al., 2019). Migration of free gas from hydrate dissociation is unlikely to reach the active portion of the TLC1 (Screaton et al, 2019). Based on these results, we evaluated the role of sedimentation and vertical fluid flow on the initiation of failure, and how strain softening during failure created a weak zone in a homogeneous sedimentary section. This weak layer now accommodates the creeping manner of the submarine landslide (Mountjoy et al., 2009). We investigate this through integration of physical property data, geotechnical laboratory experiments, and numerical models.

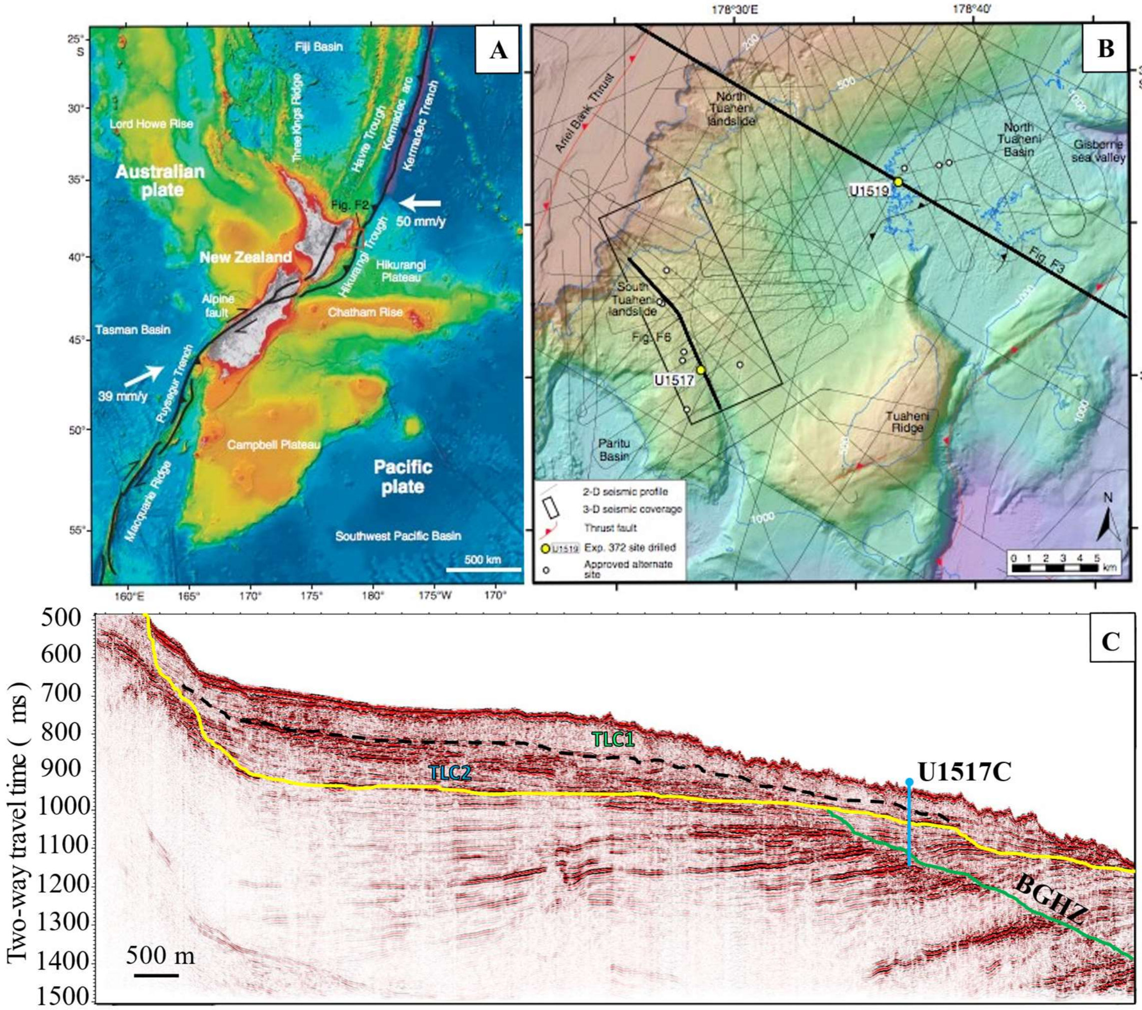

Figure 3.1: A) Topography and bathymetry map of New Zealand, showing the location of the Tuaheni Landslide Complex (TLC). B) Location of seismic lines and surveys over the TLC and the IODP Expedition 372 Site U1517. C) Two-way travel time seismic section with interpreted horizons of interest including TLC1 and TLC2. The yellow line denotes the base of the landslide debris, and the green line denotes the base of the gas hydrate stability zone (Barnes et al., 2019).

3.3 Methods

3.3.1 Sedimentation- Fluid Flow Modeling

High sedimentation rates in settings with low permeability sediments can generate fluid overpressure (P*, pressure in excess of hydrostatic) (Gibson, 1958) that can drive slope failure (Dugan and Flemings, 2000). To address the role of overpressure in initiation of the TLC, we model overpressure evolution during deposition of a 1D sedimentary section that reflects conditions at IODP Site U1517,

$$\frac{\partial P^*}{\partial t} = c_v\left(\frac{\partial^2 P^*}{\partial z^2}\right) + \gamma' \frac{\partial h}{\partial t}, \quad (3.1)$$

where c_v is the coefficient of consolidation, γ' is the effective unit weight of the sediments, and ∂h/∂t is the sedimentation rate in mm/yr. Effective unit weight is the difference between the saturated unit weight and the unit weight of water ($[\gamma' = \gamma_s - \gamma_w = (\rho_b - \rho_w)g]$). Based on core and logging data we use a fluid density, ρ_w, of 1024 kg/m^3 for seawater and a bulk density, ρ_b, of 1830 kg/m^3. We determine c_v from the permeability of the sediment, the dynamic viscosity of the fluid (water) and the storativity (St) of the system,

$$c_v = \frac{k}{\mu * St}. \quad (3.2)$$

In situ permeability is estimated from constant-rate-of-strain consolidation experiments (Dugan et al., 2018). Storativity is calculated from porosity, bulk compressibility, and fluid compressibility (Dugan and Flemings, 2002),

$$St = \frac{\varphi_0 * \beta}{1-\varphi_0} + \varphi_0 * \beta_f. \quad (3.3)$$

We determine the bulk compressibility and initial porosity values by performing a regression of measured porosity and hydrostatic vertical effective stress (Hubbert and Rubey, 1959; Dugan and Flemings, 2000)

$$\varphi = \varphi_0 * e^{-\beta(S_v - \rho_w g z - P^*)}. \quad (3.4)$$

Total vertical stress (S_v) is determined by integrating bulk density data (Barnes et al., 2019). We assume hydrostatic conditions (P* = 0) based on measured pressure at Site U1517 (Barnes et al., 2019, Pecher et al., 2019). For our regression we look at the upper 10 m of sediment as we hypothesize that failure occurred when the sediments were buried at shallow depths. Our regression yields a bulk compressibility value of $5.68e^{-6}$ Pa^{-1} ($R^2 = 0.75$) (Figure 3.2).

Based on the range of permeabilities within our intervals of interest we determine a range of c_v values. We present results for a constant coefficient of consolidation of $3.5e^{-8}$ m^2/s that aligns with representative values of bulk compressibility and permeability.

Sedimentation rates are based on biostratigraphy and radiocarbon dating of materials from Site U1517 (Barnes et al., 2019). Sedimentation rates range from 0.487 mm/yr to 79.474 mm/yr. The model employs a no-flux basal boundary condition and a hydrostatically pressured upper boundary condition (seafloor).

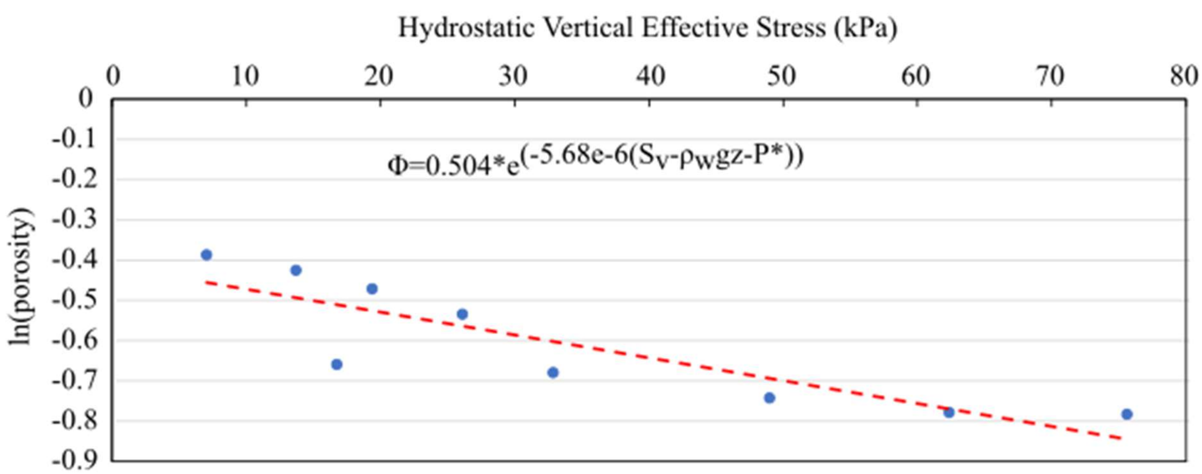

Figure 3.2: Regression of the natural log of porosity against the hydrostatic vertical effective stress at the porosity data points' respective depths ($R^2 = 0.752$). The regression provides the bulk compressibility beta value for the upper 10 m of deposition of the landslide.

3.3.2 Direct Simple Shear (DSS) Experiments

We completed DSS experiments on five core samples taken from Site U1517. These samples range in depths from 38.84 m below seafloor (mbsf) to 181.09 mbsf. We use standard testing procedures for all DSS experiments (ASTM International, 2007).

3.3.2.1 Sample Preparation

After collection on IODP Expedition 372, each sample was stored in a sealed, refrigerated core liner. To prepare a sample for experiments, a sample is removed from the liner and trimmed to the appropriate size for the experiments. We trim samples to right cylinders of either 66.29 mm (diameter) by 18.57 mm (height) or a 50.80 mm (diameter) by 18.80 mm (height). The sample is then covered by a rubber membrane and placed into the DSS rings and apparatus. Each sample is maintained at fully saturated conditions after preparation and throughout the experiment.

3.3.2.2 Consolidation

Prior to shearing, each sample is incrementally loaded to its pre-consolidation stress assuming in situ pore pressure is hydrostatic, which is based on a hydrostatic pressure measurement at Site U1517 (Barnes et al., 2019). See Appendix A for the final pre-consolidation stress for each experiment. Time after each load increment is set to ensure pore pressure dissipation between load steps.

3.3.2.3 Shear Deformation

After samples are consolidated to the estimated pre-consolidation stress, the samples are sheared at a constant rate (0.0051 mm/min). During shear, each sample is held at a constant height, which allows us to calculate the pore pressure generated during shear (Δus),

$$\Delta us = \sigma'_{nc} - \sigma'_{n} \tag{3.5}$$

where σ'_{nc} is maximum pre-shear normal stress, and σ'_{n} is normal stress during shear (ASTM International, 2007).

3.3.2.4 Shear Analysis

Data from the DSS experiments are processed to provide void ratio, shear strength, and pore pressure generation of each sample as a function of shear strain (ASTM International, 2007). Peak shear strength is defined as the maximum shear strength value (Figure 3.3).

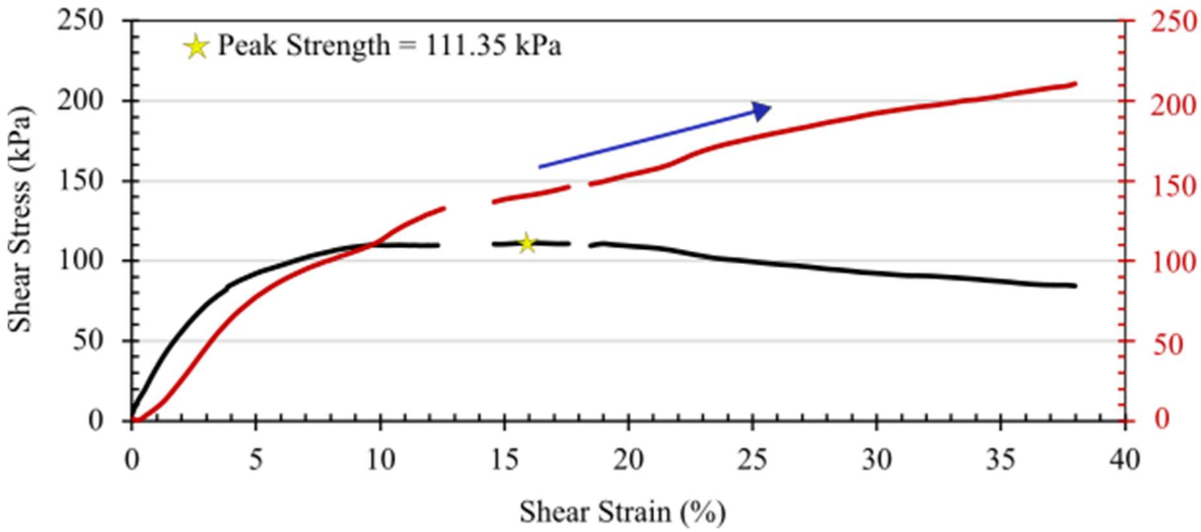

Figure 3.3: Direct simple shear (DSS) experiment data from a core sample from 38.84 mbsf. Strength data show peak shear strength at 16.20% strain followed by strain weakening with increasing strain. Shear induced pore pressure continues to be generated after the peak strength is reached.

3.4 Results

3.4.1 Sedimentation-Fluid Flow Model Results

We model 107,500 years of sedimentation and fluid flow to gain insight into the evolution of overpressure at Site U1517 for the deposition of 100 m of sediment. We specifically focus on intervals within and outside of the TLC (30 mbsf, 37 mbsf, 38.84 mbsf, 59 mbsf, and 75 mbsf). We investigate the 30 mbsf horizon because penetrometer measurements confirm a low undrained shear strength of 4.9 kPa (Figure 3.2) (Barnes et al., 2019, Couvin et al., 2020). We evaluate the 37 mbsf horizon as this is interpreted to be the decollement accommodating shear deformation at the bottom of TLC1, and it has a penetrometer-based undrained shear strength of 83.4 kPa (Figure 3.4) (Mountjoy et al., 2014). The third horizon of interest is 38.84 mbsf, which coincides with the depth of one of the samples we use in our DSS experiments, and which has a low undrained shear strength determined from the penetrometer data (78.5 kPa). The 59 mbsf horizon is evaluated as it is the interpreted base of the Tuaheni Landslide Complex (Mountjoy et al., 2014). Our fifth model horizon at 75 mbsf provides a reference for where slope failure has not occurred, and a reference for where there is no gas hydrate presence to impact overpressure (Barnes et al., 2019). We present model results in terms of normalized overpressure (λ^*) as it allows comparison of different horizons and can be quickly related to the factor of safety. Normalized overpressure is the overpressure divided by the overburden stress.

With our constrained sedimentation rates and coefficient of consolidation, we predict near-hydrostatic conditions ($\lambda^*=0$) for the present day (Figure 3.5). This model result is consistent with direct hydrostatic pressure measurement at 80 mbsf (Figure 3.5), validating our model approach. With a validated model, we investigate the evolution of the system during deposition and burial.

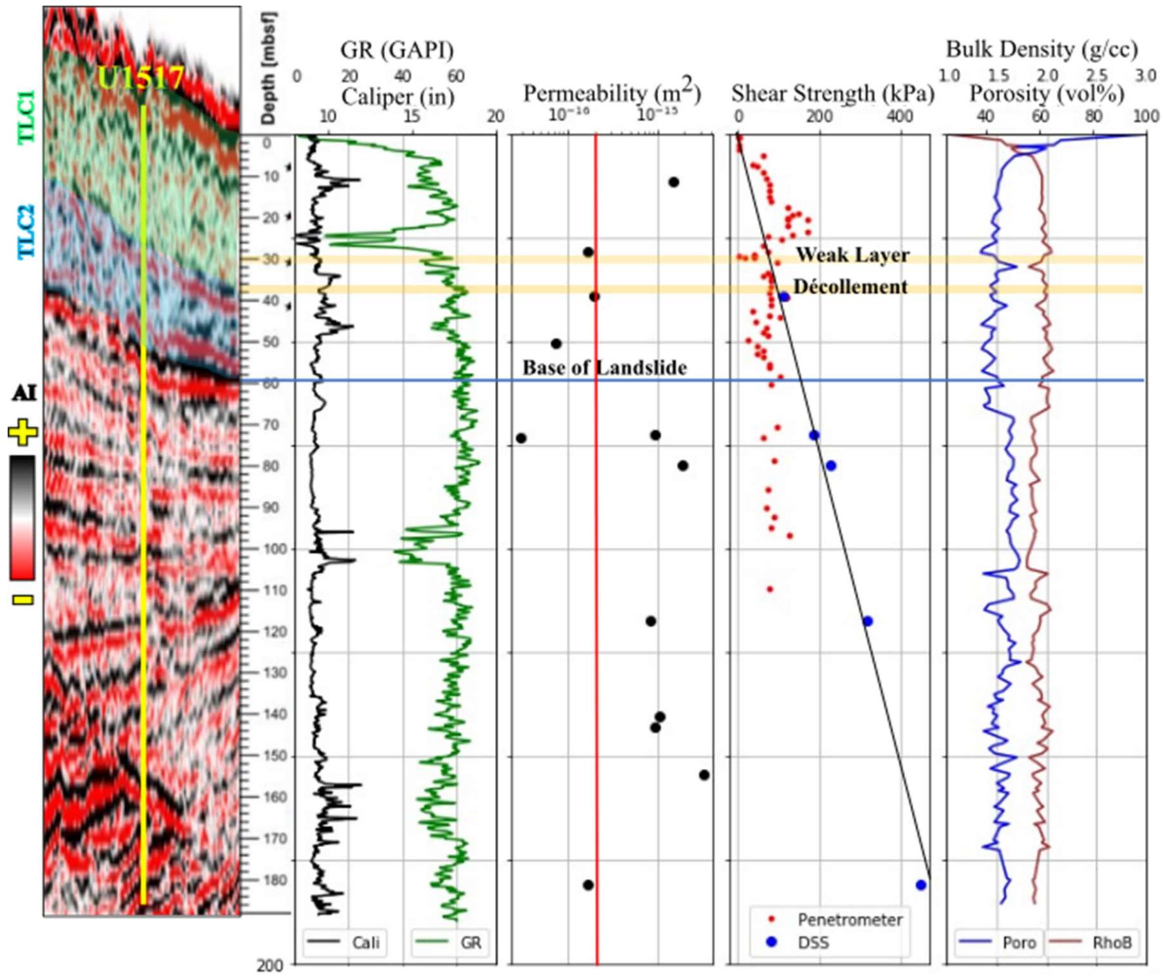

Figure 3.4: Site U1517 well log and seismic data. Track 1 provides an annotated seismic section showing the TLC1 and TLC2 sections. Track 2 provides the caliper (black) and gamma ray (green) logs. Track 3 provides the permeability measurements (solid black dots) and the comparative permeability value used in our model (red line). Track 4 provides DSS-measured peak shear strength (blue) and core-based penetrometer peak shear strength measurements (red). The black line is a linear regression of our DSS peak shear strengths with depth. Track 5 documents the porosity (blue) and the bulk density (brown) data. Defined across all tracks are the interpreted weak horizon from (Couvin et al., 2020), décollement (Barnes et al., 2019), and the base of the landslide complex (Mountjoy et al., 2014).

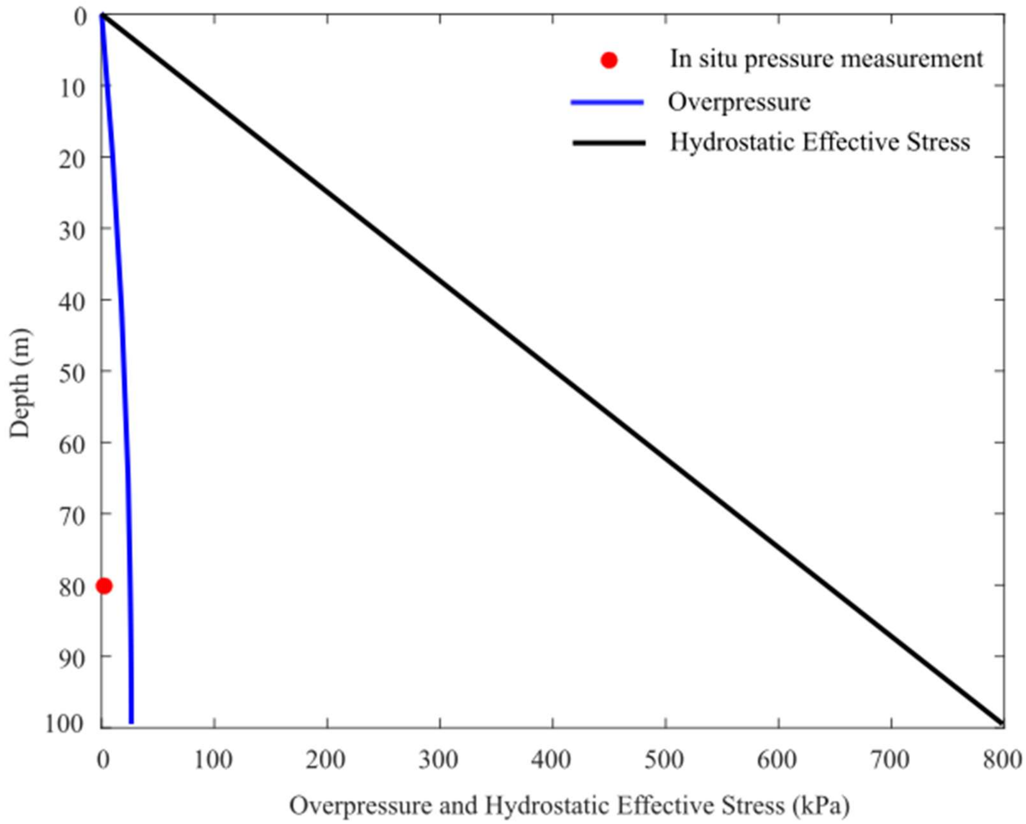

Figure 3.5: Model for modern-day pressure regime showing absolute overpressure values with depth. An in-situ pressure measurement (solid red dot) from Site U1517 also indicates nearly hydrostatic conditions.

At the onset of deposition for the 30 mbsf horizon, normalized overpressure increases from 0.45 to 0.90 at 24,603 yrs BP (Figure 3.6). Normalized overpressure for this horizon remains greater than 0.90 until 24,440 yrs BP and reaches a peak normalized overpressure of 0.95 at 24,457 yrs BP (Figure 3.6). The increasing normalized overpressure coincides with a sedimentation rate of 26.788 mm/yr. The normalized overpressure begins to decline when the sedimentation rate drops to 7.668 mm/yr.

Normalized overpressure on the interpreted decollement (37 mbsf) (Mountjoy et al., 2014) increases from 0.39 at deposition to 0.90 at 24,822 yrs BP (Figure 3.6). Normalized overpressure in this horizon remains above 0.90 until 24,792 yrs BP, reaching a maximum of 0.98 at 24,801 yrs BP before decreasing to 0.82 (Figure 3.6). After some dissipation the normalized overpressure on this horizon begins to increase to a relative maximum of 0.89 at 24,457 yrs BP (Figure 3.6). Normalized overpressure in the 38.84 mbsf horizon reaches a maximum of 0.95 at 24,801 yrs BP and remains above 0.90 normalized overpressure from 24,815 yrs BP to 24,795 yrs BP (Figure 3.6). This horizon also experiences a dissipation of pressure back down to 0.80 normalized overpressure. The normalized overpressure for this horizon then increases again to a value of 0.88 at 24,457 yrs BP (Figure 3.6). For the 37 and 38.84 mbsf horizons, the absolute normalized overpressure maximums coincide with the end of the highest sedimentation rate of 79.474 mm/yr. The horizons' second local maxima coincide with the next drop in sedimentation rates from 26.788mm/yr to 7.668 mm/yr. Both horizons only exhibit increases in normalized overpressure during the intervals where the sedimentation rates are 79.474 and 26.788 mm/yr.

The fourth horizon (59 mbsf), which is the base of the landslide debris, shows an increase in normalized overpressure from 0.16 at 24,877 yrs BP to 0.59 at 24,801 yrs BP (Figure 3.6). The normalized overpressure reaches a maximum value of 0.72 at 24,457 yrs BP, and then steadily decreases with time (Figure 3.6). Our model results of the normalized overpressure for the 75 mbsf horizon show a similar trend as that of the 59 mbsf interval with two intervals of increasing normalized overpressure occurring before a decrease to background pressure. The 75 mbsf horizon reaches a maximum normalized overpressure value of 0.61 at 24,457 yrs BP (Figure 3.6). Our simulations show that the normalized overpressures for both horizons increase most rapidly during the sedimentation interval coinciding with a sedimentation rate of 79.474 mm/yr. However, the maximum normalized overpressures reached by these horizons coincide with the end of the 26.788 mm/yr sedimentation rate interval.

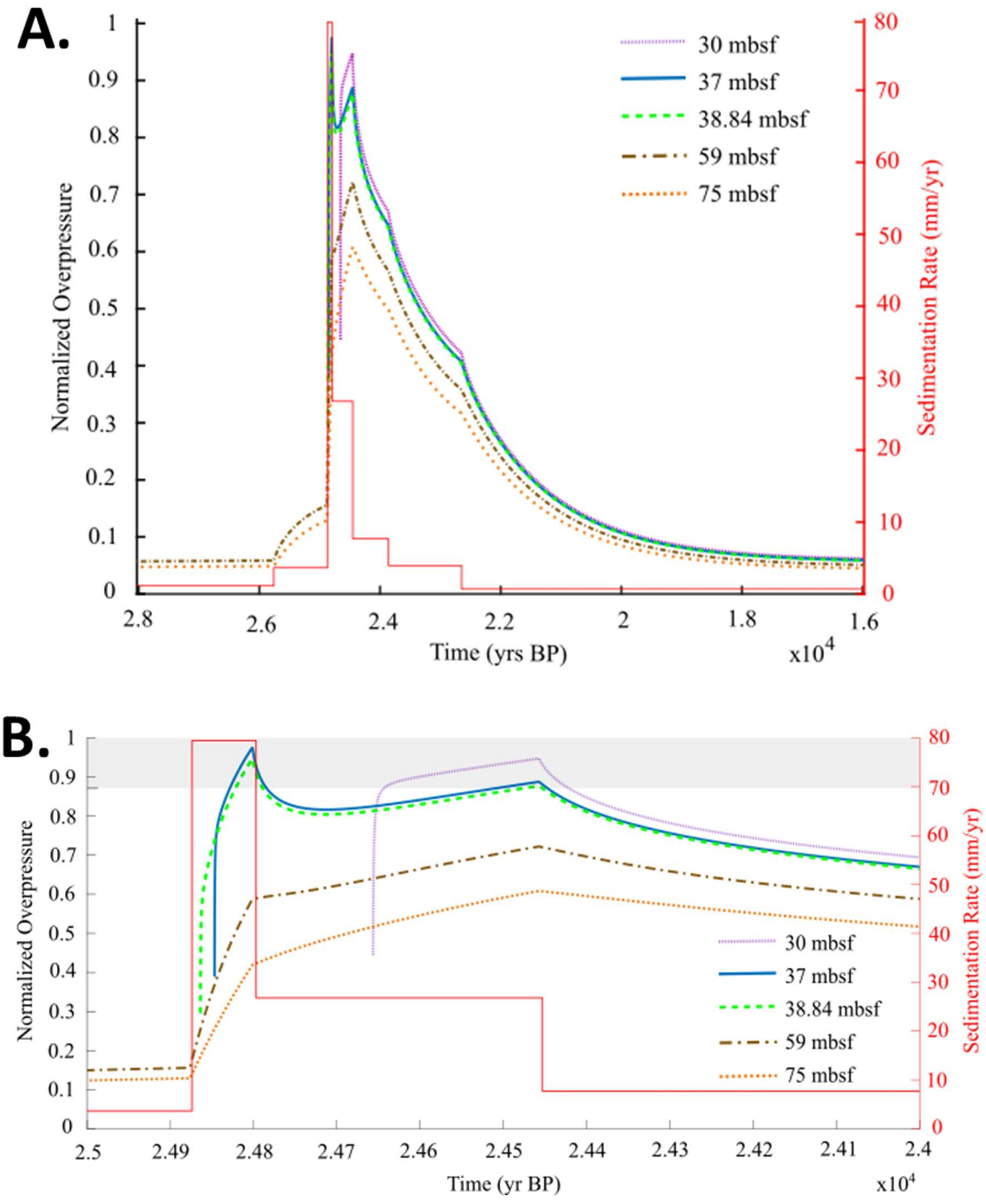

Figure 3.6: A) Simulated normalized overpressure (left y-axis) at 30 mbsf, 38.84 mbsf, 37 mbsf, 59 mbsf, and 75 mbsf, and documented sedimentation rate (right y-axis) as functions of time before present. B) A zoomed in look at the model normalized overpressure for 25,000-24,000 BP. The grey filled portion denotes the area of failure as defined by a normalized overpressure greater than 0.87.

3.4.2 DSS Experiment Results

Data from the DSS experiments document the shear strength of the sediments pre- and post-failure. DSS measurements at 38.84 mbsf show a peak shear strength of 111 kPa and a decrease in shear stress with increasing strain (Figure 3.7). Our sample at 72.26 mbsf reaches a peak shear strength of 187 kPa before decreasing with increasing strain. Our DSS results for the sample at 79.73 mbsf provide a peak shear strength of 227 kPa with the shear stress decreasing for the remainder of the experiment. Our final experiments at 117.21 mbsf and 181.09 mbsf give peak shear strengths of 318 kPa and 448 kPa, respectively, and then the shear stress decreases with increasing strain. Our peak strength data show a linear trend with depth (Table 3.1 and Figure 3.2). A linear regression of the data with an intercept of 0 defines a shear strength gradient of 0.39 kPa/m (R^2 = 0.99) (Figure 3.2).

Table 3.1: A) Values for peak shear strength, strain at peak shear strength, and shear induced pore pressure generated at the strain of peak shear strength. B) Values for maximum shear strain reached for each core sample, the shear strength at the maximum shear strain, and the shear induced pore pressure generated at the maximum shear strain.

A.	Peak Shear Strength Values		
Depth (mbsf)	Maximum Shear Strength (kPa)	Strain @ Maximum Shear Strength (%)	Pore Pressure @ Maximum Shear Strength (kPa)
38.84	111	16.20	141
72.26	187	14.16	254
79.73	227	16.69	261
117.21	318	14.29	381
181.09	448	12.96	618

Table 3.1 contd.

B.	**Peak Shear Strain Values**		
Depth (mbsf)	**Maximum Shear Strain (%)**	**Shear Strength @ Maximum Shear Strain (kpa)**	**Pore Pressure @ Maximum Shear Strain (kPa)**
38.84	37.99	85	211
72.26	43.69	104	473
79.73	42.11	135	477
117.21	41.04	185	698
181.09	38.56	242	1172

In addition to peak shear strength, our experiments document strain weakening behavior for all samples (Figure 3.7). The sample at 38.84 mbsf has a 23% decrease in strength from the peak strength (111 kPa) to the final strength at the completion of the experiment (85 kPa) (Table 3.2). The 72.26 mbsf sample has a shear strength drop of 44% from peak strength (187 kPa) to shear strength at maximum strain (104 kPa) (Table 3.2). The 79.73 mbsf sample again exhibits a 41% decrease in shear strength from peak strength (227 kPa) to shear strength at maximum strain (135 kPa) (Table 3.2). At 117.21 mbsf our DSS experiment constrains a 42% decrease in shear strength from the peak strength (318 kPa) to the shear strength at maximum strain (185 kPa) (Table 3.2). For the 181.09 mbsf sample, the peak shear strength drops from 448 kPa (peak shear strength) to 242 kPa (shear strength at maximum strain) during the experiment, which is a 46% drop in shear strength (Table 3.2).

Table 3.2: We give the sample data for each direct simple shear experiment analyzed in this study and include the respective setup parameters designated for each experiment.

Direct Simple Shear Experiment Parameters						
IODP Core Boring Number	Depth (mbsf)	Sample Designation	Minimum Normal Load (psf)	Maximum Normal Load (psf)	Number of Consolidation Steps	Duration (days:hrs:mins:sec)
U1517C-7F4	38.84	DSS026	100	7142	7	06:01:03:32
U1517C-15H5	72.26	DSS027	200	13638	7	06:01:11:32
U1517C-15H7	79.73	DSS028	200	14940	7	06:01:06:02
U1517C-20F4	117.21	DSS029	200	21554	8	07:13:11:10
U1517C-35F3	181.09	DSS030	400	33375	8	07:13:11:36

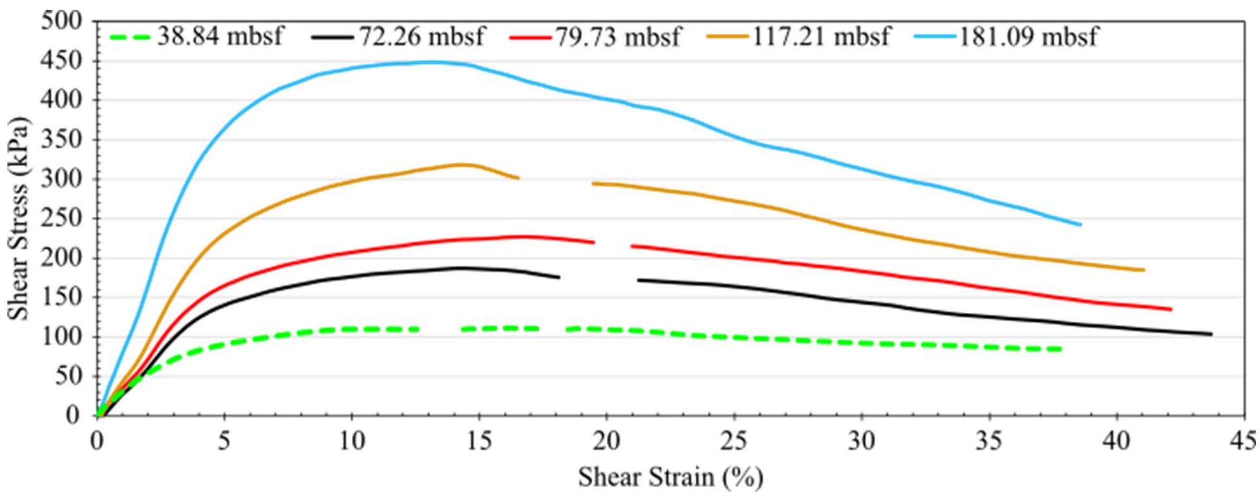

Figure 3.7: Direct simple shear (DSS) stress results for all core samples. The result for 38.84 mbsf is of particular interest because it captures data on the sediments inside the TLC. Gaps in data are the result of equipment malfunction.

Our experiments also document that all samples generate excess pressure during shear (Figure 3.8). Our sample at 38.84 mbsf generates a pore pressure of 211 kPa at a shear strain of 38%. The sample at 72.26 mbsf generates pore pressures up to 473 kPa at 44% shear strain. The following sample at 79.73 mbsf induces a pore pressure of 477 kPa at 42% shear strain. As we continue deeper, the sample at 117.21 mbsf generates pore pressures up to 698 kPa at 41% shear strain. The deepest sample at 181.09 mbsf produces a pore pressure of 1172 kPa at 39% shear strain. In each case, the absolute pore pressure generation occurs after reaching failure and the peak shear strength (Figure 3.9). Our experiments also document that after failure, the shear induced pore pressures and their gradients increase with depth. After failure the shear-induced pore pressure gradient for the 38.84 mbsf sample is 3.24 kPa/%strain (Figure 3.9). Our sample at 72.26 mbsf provides a shear induced pore pressure gradient of 9.4 kPa/%strain (Figure 3.9). In addition, at the maximum strain reached by each experiment we observe increasing pore pressures. This provides first-order confirmation of continued pore pressure generation with increasing strain.

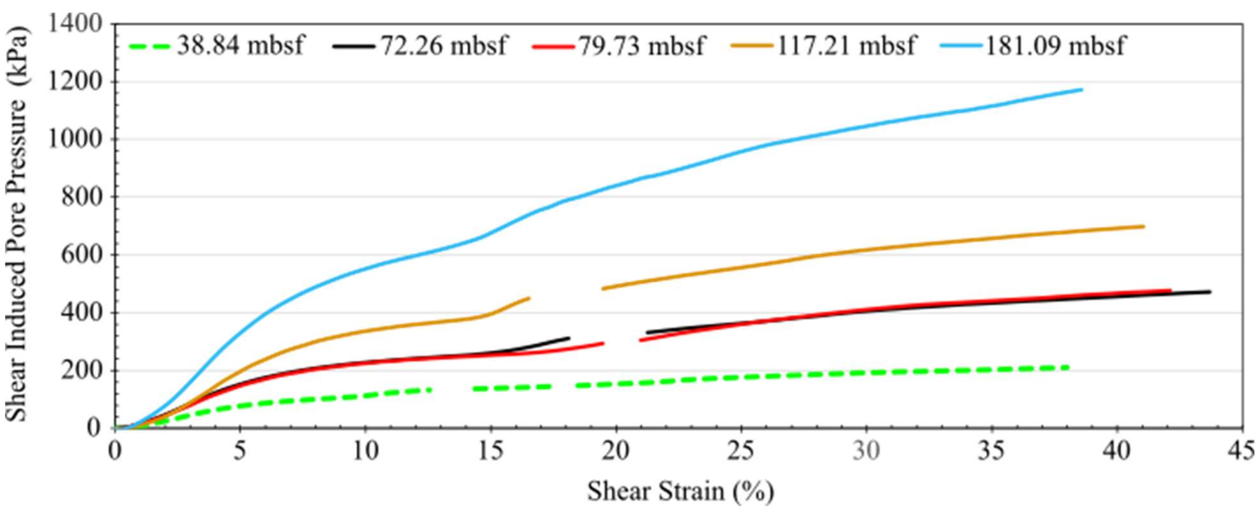

Figure 3.8: Direct simple shear (DSS) induced pore pressure for all core samples. Notice that the samples deeper and outside of the TLC have an inflection point where the shear induced pore pressure gradient increases. Gaps in data are the result of equipment malfunction.

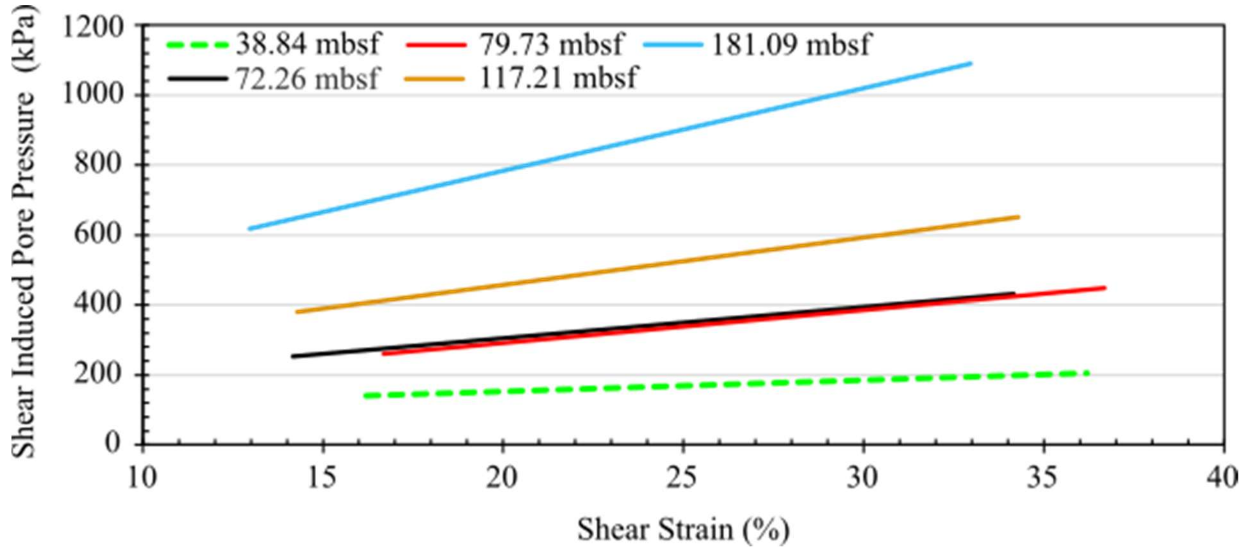

Figure 3.9: Shear-induced pore pressure gradients determined from the shear strain at peak shear strength to 20% strain past the peak strength for all core samples.

3.5 Discussion

Our sedimentation-fluid flow models predict that the TLC is a near hydrostatically pressured system today. This is broadly consistent with the hydrostatic pressure measurement at 80 mbsf (Pecher et al., 2018). This hydrostatic result supports our assumption of hydrostatic conditions used in our calculation of vertical effective stress for our compressibility regression (Figure 3.3).

With our hydrostatic assumption validated we can discuss the implications of changes in β and k on our model results. In our models we employ a constant coefficient of consolidation (c_v = $3.5e^{-8}$ m/s^2) which is compatible with the ranges for bulk compressibility and permeability for this system. Our analysis of bulk compressibility is based on the shallow, hydrostatic conditions which are consistent with our model results. For permeability, we assume a simple value consistent with permeability measurements while honoring system complexities and accounting for the harmonic average of those permeabilities (Freeze and Cherry, 1979). Through numerical experiments, we find that subtle changes in the bulk compressibility and permeability (e.g., due to local, small-scale heterogeneity) values may be important for the localizing of failure to distinct horizons.

To better understand the role of sedimentation and overpressure in failure, we employ a straightforward, infinite slope factor of safety (FS) evaluation. (Flemings et al., 2008),

$$FS = \frac{\tan \varphi_f}{\sin\theta \cos\theta}(cos^2\theta - \lambda^*). \qquad (3.6)$$

For the TLC, the slope (θ) ranges from 1.5 – 4.0° (Mountjoy et al., 2014), and if we assume a friction angle, φ_f, of 30°, consistent with undrained clay sediments, we can achieve failure (FS < 1) with P* greater than 0.87 (θ = 4°) and 0.95 (θ = 1.5°).

Beginning with the shallowest horizon at 30 mbsf, we predict failure (λ* > 0.87) from deposition until 224 years after deposition. This horizon reaches failure upon deposition, after which the increase in overpressure slows dramatically, while still meeting conditions for failure for an extended period.

At 37 mbsf, normalized overpressure required to generate failure occurs in two separate time intervals. The first failure occurs during the 79.474 mm/yr sedimentation rate interval and lasts for 44 years. The second instance of failure occurs for about 69 years at the end of the 26.788 mm/yr sedimentation rate interval. The total time of failure for this horizon is about half of that of the 30 mbsf horizon.

Similarly, the horizon at 38.84 mbsf exhibits two periods where normalized overpressure is high enough to drive failure. This horizon fails initially upon deposition during the highest sedimentation interval and is in a state of failure for about 33 years before entering a period of no failure. A second period of failure then lasts for about 27 years. This horizon's total time of failure is shorter than the 37 mbsf horizon's failure duration and much shorter than that of the 30 mbsf horizon.

The 38.84 mbsf model horizon's predicted failure is reinforced by positive feedback with our strain weakening and shear-induced pore pressure genesis DSS experiment results for our 38.84 mbsf sample. Our DSS experiments show that this and all other samples exhibit strain weakening. At 38.84 mbsf there is a 24% decline in shear strength after failure. Deeper samples (i.e., 72.26 mbsf and deeper) exhibit higher percent drops in strength (up to 46%), meaning there is potential for other horizons to strain weaken more than the 38.84 mbsf horizon. During shear we observe pore pressure generation in excess of 200 kPa. The 30 and 37 mbsf horizons are shallower than the 38.84 mbsf sample and most likely would follow the trend of our experiments and generate less shear induced pore pressure. From this, we discern that upon failure at 38.84 mbsf the process of weakening the sediment and pressurizing it through shear strain begins.

According to our model predictions, both the 59 mbsf and 75 mbsf horizons never reach failure conditions solely from sedimentation-generated overpressure. The 59 mbsf is interpreted as the base of the TLC, indicating that deformation on this horizon has occurred. Based on this, we interpret an external force may have been required for this horizon to fail (e.g, earthquake-induced ground motion) (Clark et al., 2019). The deepest modeled horizon at 75 mbsf shows neither predicted nor interpreted signs of failure, so we interpret that this horizon has not experienced failure.

With our prediction that all sediments between 30 mbsf and 38.84 mbsf generated overpressure sufficiently for failure upon deposition ($P^* \geq 0.87$), we now look at potential differences between the relatively homogeneous horizons. We predict that the 30 mbsf horizon was in a state of failure for the longest amount of time and therefore has likely experienced the most shear strain. We interpret that this horizon's extremely low shear strength is due to extensive strain during an extended period of failure. Although the 30 mbsf horizon experienced the longest predicted failure, the other two horizons also experienced failure that left them in a current non-failure, but weakened, state.

We explore the occurrence of an extended failure period on these weak horizons at 30 to 39 mbsf through failure during deposition as a positive feedback via shear-induced pressure genesis. Combining our shear experiments with our models we envision a system where failure during high sedimentation rates is likely to be driven further with the generation of pore pressure during the shear failure. In addition, failure could be even more extensive with effects of pressure increase from fluid influx from either deep pressure sources or transferred from lateral pressures (Dugan and Flemings, 2000; Gross et al., 2018). With the relatively high permeability of the system, however, drainage during modern, low sedimentation rates allowed the TLC to stabilize and dissipate this failure-generated overpressure. In this way we identify a mechanism in which failure upon deposition and pore pressure generation allow for extensive failure that leads to strain weakened layers that are still able to later reach nearly hydrostatic conditions.

In comparison of our DSS experiments and penetrometer data, we note consistencies and differences. Above 30 mbsf the linear regression of our experimental peak shear strength is lower than the penetrometer data (Figure 3.2). As we enter the weak layer and model predicted zone of failure, the linear regression and our 38.84 mbsf shear strength measurement align closely with the penetrometer data (Figure 3.2). These data, however, begin to diverge below 40 mbsf where the penetrometer data reveal lower shear strengths than our peak strength regression. These shallow discrepancies might be due to small-scale heterogeneity and deeper differences partly explained by the inability of accurate penetrometer measurements to reliably constrain undrained shear strength. Our linear regression predicts a peak shear strength with depth gradient of 0.39 kPa/m. This increase in shear strength with depth is consistent with shear strength gradients associated with active continental margins where active tectonic processes, such as subduction and earthquakes, occur (Sawyer and DeVore, 2015). The shear strength, in kPa, versus the vertical effective stress, in kPa, establishes a gradient of 0.29, which is consistent with sediments of normal shear strength and not the high shear strength associated with an active margin environment (Sawyer and DeVore, 2015) (Figure 3.10).

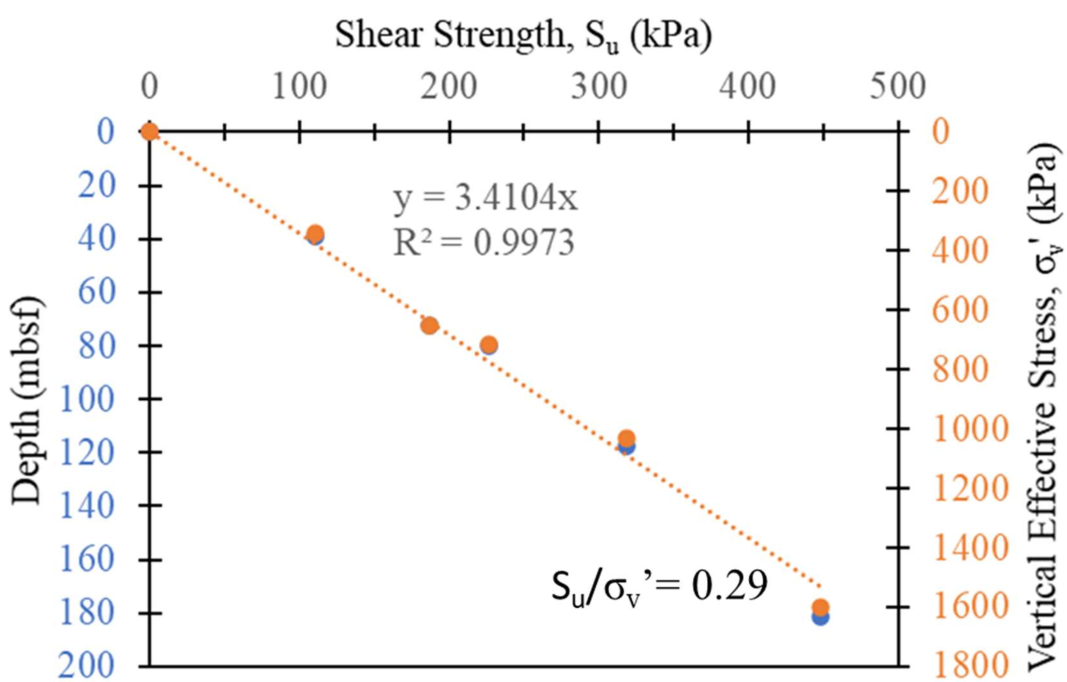

Figure 3.10: Regression of experimentally derived shear strength data producing a shear strength gradient for the TLC (orange).

3.6 Conclusion

Throughout this study we have investigated a deforming mechanism driving the Tuaheni Landslide Complex's current failure. We specifically focused on the plausibility of fluid flow and rapid sedimentation producing sufficient pressure to destabilize the submarine landslide. We identified a feedback process by which high sedimentation rates can create slope failure upon sediment deposition. Shear strain accumulated during initial failure weakens those sediments and generates pore pressure that can extend the failure duration. This ultimately creates the observed weak layer.

In identifying this stepwise process, our modeling shows that it is possible for initial failure of the TLC to have occurred at the 37 mbsf layer, and our experimentation has discovered that the TLC sediments are strain weakening. Additionally, this study addresses the question surrounding fluid input and the lack thereof to drive overpressure. We have discovered that with such high sedimentation rates as occurred during the deposition of the TLC, coupled with moderate permeabilities, a mass influx of fluid or gas is not required to bring the sediments to failure. Additionally, the experimental results suggest that the generation of pore pressure during shear can act to sustain failure. Differences in rheology are not required for failure in this case, therefore illuminating a process for creating weakened zones within an otherwise homogeneous system.

Although we have focused our research efforts on a highly tested and dynamic system, this work has implications for similar environments of high mud percentage sediments being rapidly deposited within a short geologic time interval. With a wide range of environments to investigate this phenomenon, there is room to further understand and defend such a process. Future work is needed at the TLC to investigate the nature of the shallowest sediments, those above 38.84 mbsf, to more accurately assess that the shallowest interval also behaves by strain weakening. Such work can be done with additional DSS experiments on those shallower sediments. The influence of characteristics such as bulk compressibility and permeability on the modeled overpressure results could support the need for a sensitivity study to best define the most accurate model inputs.

CHAPTER 4

CONCLUSIONS AND FUTURE WORK

Submarine landslides pose a great hazard to onshore and offshore infrastructure, as well as to human life. Numerous occasions in recent history show the destructive nature of submarine landslides and have fueled widespread scientific research to understand their failure histories and failure potential. IODP Expedition 372 aimed to understand the Tuaheni Landslide Complex (TLC) on the active continental margin offshore the east coast of the North Island of New Zealand. One specific aim of Expedition 372 was to define the processes that initiated the TLC including the formation of a weak layer facilitating creep-like behavior of the slide complex. Our study took the core samples and logging data from this expedition and combined it with previously identified burial history data to provide an answer to this aim of IODP Expedition 372.

When combining the results from our TLC research, we present a means by which a notably homogeneous system initially can fail, form a weak layer, and return to hydrostatic conditions. Our numerical modeling identifies how a failure initializes in a zone bereft of lithologic and mineralogic variability. Initial failure then provides sufficient overpressure to continue failure for decades of time. An extended failure period is exacerbated by the strain weakening nature of the sediments as well as the increase in pore pressure generated by shear strain. We identify this process as a feedback mechanism that ultimately produces a weakened layer, where failure has occurred, that can reach hydrostatic conditions when sedimentation rates slow.

This fundamental finding begins with our investigating the effects of sedimentation coupled with fluid – flow properties on the initiation of failure of the TLC.

Through our 1D model and analysis we discover that with reasonable values for permeability and bulk compressibility, rapid sedimentation is enough for failure upon deposition of the sediments on a shallow slope. Our model reveals that deposition during and after the period of the highest sedimentation rate provides overpressure values up to 90% of lithostatic overburden which satisfies the requirements for slope failure, given the TLC's gentle slope. This failure occurs at depths between 30-39 mbsf, coinciding with recent findings supporting the existence of a weak layer at this depth. Our study further reveals that failure in this shallow zone happened for an extended period, lending to the development of the observed weak layer.

A result of the progressive failure duration shown at the 30-39 mbsf interval following such rapid sedimentation periods is the additional strain that weakened this zone. The progressive failure durations are on the order of decades to centuries, implying a simultaneously extended period of submarine landslide movement. The amount of accumulated shear strain during this time could be enough to produce the weak layer existing today. The following slow in sedimentation rates and termination of a rapid failure period allowed overpressure to dissipate. We now see that the simulated overpressure reaches nearly hydrostatic conditions for today's environment which matches the in-situ pressure measurement from IODP Expedition 372.

At today's conditions, we use the core samples from Expedition 372 to characterize the bulk physical behavior of the TLC upon and after failure. Through this work we have furthered the understanding of the failure evolution of the TLC, including providing a mechanism driving failure which can be applied to other shallowly dipping slopes in subtropical and tectonically active environments, for example, the Santa Barbara Basin in California. With our findings, these environments include homogeneous sediment systems with high sedimentation rates, such as those that occur at large river deltas. Furthermore, the nature of the sediments to consider for similar investigations are clay rich with a primarily smectite composition of 50 wt%. Additionally, the strength character of these sediments within and below the interpreted active submarine landslide are strain softening. Additionally, they also exhibit increasing pore pressure development with shear strain. In this way, a failure initialized upon deposition will resultingly weaken the sediments, and the increase in pressure from strain will lengthen the failure time. This corresponds with our observations of extended failure times identified through our model. Initial failure driven by extremely high sedimentation rates is extended by the strain weakening nature of the sediments. By this process we achieve an induced weak layer observed presently at a time where overpressure has dissipated to hydrostatic levels.

Our investigation revealed the ability and likelihood for the failure and development of a submarine landslide and consequent weak layers within a homogeneous system. Future work is needed to constrain the additional impetus needed to bring the TLC to failure and what type of failure is most likely to occur. Strain reconstructions would assist in determining the nature of initial failure of the TLC and whether it was catastrophic or non-catastrophic. Constraining the likelihood of the type of future failure accounts for constraining the potential hazard from future slope failures. This could be performed by advancing monitoring systems of the TLC through 4D bathymetric models. 4D monitoring would provide active data to interpret the current occurrence of slow deformation of the TLC and high-resolution bathymetry models can provide knowledge on the TLC's total accommodated strain to date.

Identifying the proximity of the TLC to current failure is additionally important to understanding its associated hazard. With shallower core available from IODP Expedition 372 for Site U1517, DSS experiments can be run to further constrain the sediment shear strength in the upper portion of the landslide above the failure location and where current penetrometer measurements identify a higher shear strength gradient. This is needed to identify if these sediments are also strain weakening and whether they would require external forces to fail. A 4D bathymetric model could be used to assess the total strain amount that has occurred at the failure horizon, providing knowledge on the degree of weakness caused by strain weakening in the sediments.

Further study on the impact of seismic accelerations on this submarine landslide failure is also integral in a conclusive assessment of the hazard of the TLC. With the TLC's proximity to the Hikurangi margin, study on its reactivity to earthquakes will help assess the likelihood of future failure given the weakening due to strain from its previous failure. A thorough study would include additional in situ pressure measurements throughout the TLC, to further constrain the current pressure state of the complex. Previous studies discuss the role of seismic activity on slope failure and failure reactivity in this region, and on this margin specifically. The TLC presents a conundrum because our analysis suggests an extremely weak layer exists within the submarine landslide and strong earthquakes, up to 7.3 M_w, have occurred since the creation of this weak layer (Figure 4.1). A key question to consider then in the story of the failure of the Tuaheni Landslide Complex is if or when a future catastrophic failure will occur. Numerous earthquakes, including a 6.6 M_w earthquake 40 km from the TLC, have provided seismic accelerations to the region for the past 60 years (Figure 4.1). Combine this with similar processes to those described by Mountjoy et al. (2018) and it appears that the TLC should have already catastrophically failed. Further research into this topic would help elucidate the immediate geohazard associated with this shallowly dipping large volume submarine landslide.

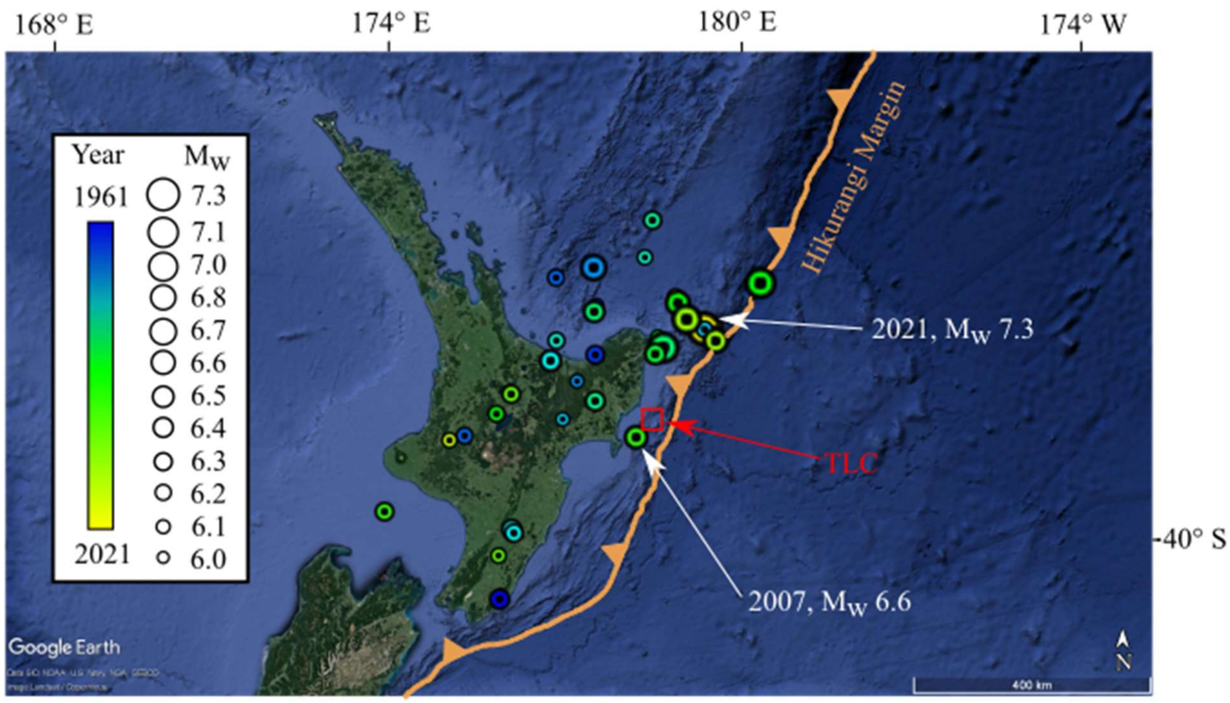

Figure 4.1: Map of earthquakes greater than 6.0 magnitude since 1960 near the North Island of New Zealand. Earthquake locations are designated by circle markers whose color coincides with year of rupture and size correlates with magnitude. Earthquake locations from USGS.

REFERENCES

ASTM International, 2007, Standard test method for consolidated undrained direct simple shear testing of cohesive soils (Standard D6528-07).

Bardet, J.-P., C. E. Synolakis, H. L. Davies, F. Imamura, and E. A. Okal, 2003, Landslide Tsunamis: Recent Findings and Research Directions: Pure and applied geophysics, v. 160, no. 10, p. 1793–1809, doi:10.1007/s00024-003-2406-0.

Barnes, P.M., Pecher, I.A., LeVay, L.J., Bourlange, S.M., Brunet, M.M.Y., Cardona, S., Clennell, M.B., Cook, A.E., Crundwell, M.P., Dugan, B., Elger, J., Gamboa, D., Georgiopoulou, A., Greve, A., Han, S., Heeschen, K.U., Hu, G., Kim, G.Y., Kitajima, H., Koge, H., Li, X., Machado, K.S., McNamara, D.D., Moore, G.F., Mountjoy, J.J., Nole, M.A., Owari, S., Paganoni, M., Petronotis, K.E., Rose, P.S., Screaton, E.J., Shankar, U., Shepherd, C.L., Torres, M.E., Underwood, M.B., Wang, X., Woodhouse, A.D., and Wu, H.-Y., 2019, Expedition 372A summary, *In* Pecher, I.A., Barnes, P.M., LeVay, L.J., and the Expedition 372A Scientists, Creeping Gas Hydrate Slides, Proceedings of the International Ocean Discovery Program, 372A: College Station, TX (International Ocean Discovery Program), doi:10.14379/iodp.proc.372A.101.2019.

Barnes, P.M., Pecher, I.A., LeVay, L.J., Bourlange, S.M., Brunet, M.M.Y., Cardona, S., Clennell, M.B., Cook, A.E., Crundwell, M.P., Dugan, B., Elger, J., Gamboa, D., Georgiopoulou, A., Greve, A., Han, S., Heeschen, K.U., Hu, G., Kim, G.Y., Kitajima, H., Koge, H., Li, X., Machado, K.S., McNamara, D.D., Moore, G.F., Mountjoy, J.J., Nole, M.A., Owari, S., Paganoni, M., Petronotis, K.E., Rose, P.S., Screaton, E.J., Shankar, U., Shepherd, C.L., Torres, M.E., Underwood, M.B., Wang, X., Woodhouse, A.D., and Wu, H.-Y., 2019, Site U1517, *In* Pecher, I.A., Barnes, P.M., LeVay, L.J., and the Expedition 372A Scientists, Creeping Gas Hydrate Slides, Proceedings of the International Ocean Discovery Program, 372A: College Station, TX (International Ocean Discovery Program), doi:10.14379/iodp.proc.372A.103.2019.

Bethke, C. M, 1986, Inverse hydrologic analysis of the distribution and origin of Gulf Coast-type geopressured zones: Journal of Geophysical Research, v. 91, p. 6535– 6545, doi:10.1029/JB091iB06p06535.

Biondi, G., G. D. Filippo and M. Maugeri, 2007, Effect of Earthquake Induced Pore-water Pressure in Clay Slopes: Proc. 4th Int. Conf. on Earthquake Geotechnical Engineering, Springer, Dordrecht, Netherlands.

Biscontin, G., J. M. Pestana, and F. Nadim, 2004, Seismic triggering of submarine slides in soft cohesive soil deposits: Marine Geology, v. 203, no. 3-4, p. 341–354, doi:10.1016/s0025-3227(03)00314-1.

Bredehoeft, J. D. and B. B. Hanshaw, 1968, On the Maintenance of Anomalous Fluid Pressures: I. Thick Sedimentary Sequences: Geological Society of America Bulletin, v. 79, no. 9, p. 1097, doi:10.1130/0016-7606(1968)79[1097:otmoaf]2.0.co;2.

Bryant, W. L., R. Camilli, G. B. Fisher, E. B. Overton, C. M. Reddy, D. Reible, R. F. Swarthout, and D. L. Valentine, 2020, Harnessing a decade of data to inform future decisions: Insights into the ongoing hydrocarbon release at Taylor Energy's Mississippi Canyon Block 20 (MC20) site: Marine Pollution Bulletin, v. 155, p. 111056, doi:10.1016/j.marpolbul.2020.111056.

Clark, K., J. Howarth, N. Litchfield, U. Cochran, J. Turnbull, L. Dowling, A. Howell, K. Berryman, and F. Wolfe, 2019, Geological evidence for past large earthquakes and tsunamis along the hikurangi subduction margin, New Zealand: Marine Geology, v. 412, p. 139–172, doi:10.1016/j.margeo.2019.03.004.

Chugh, A. K., and J. L. V. Thun, 1985, Pore pressure response analysis for earthquakes: Canadian Geotechnical Journal, v. 22, no. 4, p. 466–476, doi:10.1139/t85-066.

Couvin, B., A. Georgiopoulou, J. J. Mountjoy, L. Amy, G. Crutchley, M. Brunet, S. Cardona, F. Gross, C. Böttner, S. Krastel and I. A. Pecher, 2020, A new depositional model for the Tuaheni landslide complex, Hikurangi Margin, New Zealand: Geological Society, London, Special Publications, v. 500, no. 1, p. 551–566, doi:10.1144/sp500-2019-180.

Crutchley, G. J., J. Elger, J. Kuhlmann, J. J. Mountjoy, A. Orpin, A. Georgiopoulou, J. Carey, B. Dugan, S. Cardona, S. Han, A. Cook, E. J. Screaton, I. A. Pecher, P. Barnes and K. Huhn, 2022, Investigating the basal shear zone of the submarine tuaheni landslide complex, New Zealand: A core-log-seismic integration study: Journal of Geophysical Research: Solid Earth, v. 127, no. 1, doi:10.1029/2021jb021997.

Dugan, B., and J. Stigall, 2010, Origin of overpressure and slope failure in the Ursa Region, northern Gulf of Mexico: Submarine Mass Movements and Their Consequences, p. 167–178, doi:10.1007/978-90-481-3071-9_14.

Dugan, B., and P. B. Flemings, 2000, Overpressure and fluid flow in the New Jersey Continental Slope: Implications for slope failure and cold seeps: Science, v. 289, no. 5477, p. 288–291, doi:10.1126/science.289.5477.288.

Dugan, B., and P. B. Flemings, 2002, Fluid flow and stability of the US continental slope offshore New Jersey from the pleistocene to the present: Geofluids, v. 2, no. 2, p. 137–146, doi:10.1046/j.1468-8123.2002.00032.x.

Fan, W., J. J. McGuire, and P. M. Shearer, 2020, Abundant spontaneous and dynamically triggered submarine landslides in the Gulf of Mexico: Geophysical Research Letters, v. 47, no. 12, doi:10.1029/2020gl087213.

Fine, I. V., A. B. Rabinovich, B. D. Bornhold, R. E. Thomson, and E. A. Kulikov, 2005, The Grand Banks Landslide-generated tsunami of November 18, 1929: Preliminary analysis and numerical modeling: Marine Geology, v. 215, no. 1-2, p. 45–57, doi:10.1016/j.margeo.2004.11.007.

Flemings, P., H. Long, B. Dugan, J. Germaine, C. John, J. Behrmann, and D. Sawyer, 2008, Erratum to “Pore pressure penetrometers document high overpressure near the seafloor where multiple submarine landslides have occurred on the continental slope, offshore Louisiana, Gulf of Mexico” [Earth and Planetary Science Letters 269/3-4 (2008) 309-32]: Earth and Planetary Science Letters, v. 274, no. 1, p. 269–283, doi:10.1016/j.epsl.2008.06.027

Freeze, R. A., and J. A. Cherry, 1979, Physical Properties and Principles, in Groundwater: Englewood Cliffs, NJ, Prentice-Hall.

Gibson, R. E., 1958, The progress of consolidation in a clay layer increasing in thickness with time: Géotechnique, v. 8, no. 4, p. 171–182, doi:10.1680/geot.1958.8.4.171.

Green, D. H., and H. F. Wang, 1986, Fluid pressure response to undrained compression in saturated sedimentary rock: Geophysics, v. 51, no. 4, p. 948–956, doi:10.1190/1.1442152.

Gross, F. et al., 2018, Free gas distribution and basal shear zone development in a subaqueous landslide – insight from 3D seismic imaging of the Tuaheni Landslide Complex, New Zealand: Earth and Planetary Science Letters, v. 502, p. 231–243, doi:10.1016/j.epsl.2018.09.002.

Haflidason, H., H. P. Sejrup, I. M. Berstad, A. Nygård, T. Richter, P. Bryn, R. Lien, and K. Berg, 2003, A weak layer feature on the northern Storegga Slide escarpment: European Margin Sediment Dynamics, p. 55–62, doi:10.1007/978-3-642-55846-7_7.

Hampton, M. A., H. J. Lee, and J. Locat, 1996, Submarine landslides: Reviews of Geophysics, v. 34, no. 1, p. 33–59, doi:10.1029/95rg03287.

Harbitz, C. B., F. Løvholt, and H. Bungum, 2013, Submarine landslide tsunamis: How extreme and how likely?: Natural Hazards, v. 72, no. 3, p. 1341–1374, doi:10.1007/s11069-013-0681-3.

Heezen, B., and C. Drake, 1964, Grand Banks slump: Geological notes: AAPG Bulletin, v. 48, doi:10.1306/bc743be1-16be-11d7-8645000102c1865d.

Hubbert, M. K., and W. W. Rubey, 1959, Role of fluid pressure in mechanics of overthrust faulting: Geological Society of America Bulletin, v. 70, no. 2, p. 115-166, doi:10.1130/0016-7606(1959)70[115:rofpim]2.0.co;2.

Imamura, F., E. Gica, T. Takahashi, and N. Shuto, 1995, Numerical simulation of the 1992 Flores tsunami: Interpretation of tsunami phenomena in northeastern Flores Island and damage at Babi Island: Pure and Applied Geophysics, v. 144, no. 3-4, p. 555–568, doi:10.1007/bf00874383.

Johnson, H. P., J. S. Gomberg, S. L. Hautala, and M. S. Salmi, 2017, Sediment gravity flows triggered by remotely generated earthquake waves: Journal of Geophysical Research: Solid Earth, v. 122, no. 6, p. 4584–4600, doi:10.1002/2016jb013689.

Koppula, S.D. and N.R. Morgenstern, 1982, On the consolidation of sedimenting clays: Canadian Geotechnical Journal, v. 19, p. 260-268, doi:10.1139/T82-033.

Kubo, Y., F. Inagaki, S. Tonai, G.-I. Uramoto, O. Takano, Y. Yamada, and the Expedition 910 Shipboard Scientific Party, 2020, New Chikyu Shallow Core Program (SCORE), Exploring mass transport deposits and the subseafloor biosphere off Cape Erimo, northern Japan: Scientific Drilling, v. 27, p. 25-33, doi: 10.5194/sd-27-25-2020.

L'Heureux, J.-S., O. Longva, A. Steiner, L. Hansen, M. Vardy, M. Vanneste, H. Haflidason, J. Brendryen, T. Kvalstad, C. Forsberg, S. Chand and A. Kopf, 2011, Identification of weak layers and their role for the stability of slopes at Finneidfjord, Northern Norway: Submarine Mass Movements and Their Consequences, p. 321–330, doi:10.1007/978-94-007-2162-3_29.

Maslin, M., M. Owen, S. Day, and D. Long, 2004, Linking continental-slope failures and climate change: Testing the clathrate gun hypothesis: Geology, v. 32, no. 1, p. 53–56, doi:10.1130/g20114.1.

Masson, D. G., C. B. Harbitz, R. B. Wynn, G. Pedersen, and F. Løvholt, 2006, Submarine landslides: Processes, triggers and hazard prediction: Philosophical Transactions of the Royal Society A: Mathematical, Physical and Engineering Sciences, v. 364, no. 1845, p. 2009–2039, doi:10.1098/rsta.2006.1810.

McIver, R., 1982, Role of naturally occurring gas hydrates in sediment transport: AAPG Bulletin, v. 66, p. 789–792, doi:10.1306/03b5a318-16d1-11d7-8645000102c1865d.

Miramontes, E., N. Sultan, S. Garziglia, G. Jouet, E. Pelleter, and A. Cattaneo, 2018, Altered volcanic deposits as basal failure surfaces of submarine landslides: Geology, v. 46, no. 7, p. 663–666, doi:10.1130/g40268.1.

Mountjoy, J. J., J. McKean, P. M. Barnes, and J. R. Pettinga, 2009, Terrestrial-style slow-moving earthflow kinematics in a submarine landslide complex: Marine Geology, v. 267, no. 3-4, p. 114–127, doi:10.1016/j.margeo.2009.09.007.

Mountjoy, J. J., I. Pecher, S. Henrys, G. Crutchley, P. M. Barnes, and A. Plaza-Faverola, 2014, Shallow methane hydrate system controls ongoing, downslope sediment transport in a low-velocity active submarine landslide complex, Hikurangi Margin, New Zealand: Geochemistry, Geophysics, Geosystems, v. 15, no. 11, p. 4137–4156, doi:10.1002/2014gc005379.

Mountjoy, J. J. et al., 2018, Earthquakes drive large-scale submarine canyon development and sediment supply to deep-ocean basins: Science Advances, v. 4, no. 3, doi:10.1126/sciadv.aar3748.

Nakamura, S., S. Gibo, K. Egashira, and S. Kimura, 2010, Platy layer silicate minerals for controlling residual strength in landslide soils of different origins and geology: Geology, v. 38, no. 8, p. 743–746, doi:10.1130/g30908.1.

Nisbet, E. G., and D. J. Piper, 1998, Giant submarine landslides: Nature, v. 392, no. 6674, p. 329–330, doi:10.1038/32765.

Pecher, I. A., P. M. Barnes, L. J. LeVay, and the Expedition 372 Scientists, 2018, Expedition 372 Preliminary Report: Creeping Gas Hydrate Slides and Hikurangi LWD: International Ocean Discovery Program, doi:10.14379/iodp.pr.372.2018.

Pecher, I. A., P. M. Barnes, and L. J. LeVay, 2019, Creeping gas hydrate slides: Proceedings of the International Ocean Discovery Program, doi:10.14379/iodp.proc.372a.2019.

Sawyer, D. E., and J. R. DeVore, 2015, Elevated shear strength of sediments on active margins: Evidence for seismic strengthening: Geophysical Research Letters, v. 42, no. 23, p. 10,216–10,221, doi:10.1002/2015GL066603.

Schulten, I., D. C. Mosher, S. Krastel, D. J. Piper, and M. Kienast, 2018, Surficial sediment failures due to the 1929 Grand Banks Earthquake, St Pierre Slope: Geological Society, London, Special Publications, v. 477, no. 1, p. 583–596, doi:10.1144/sp477.25.

Screaton, E. J., M. E. Torres, B. Dugan, K. U. Heeschen, J. J. Mountjoy, C. Ayres, P. S. Rose, I. A. Pecher, P. M. Barnes, and L. J. LeVay, 2019, Sedimentation controls on methane-hydrate dynamics across Glacial/interglacial stages: An example from International Ocean Discovery Program Site U1517, Hikurangi Margin: Geochemistry, Geophysics, Geosystems, v. 20, no. 11, p. 4906–4921, doi:10.1029/2019gc008603.

Solheim, A., R. Bhasin, F. V. De Blasio, L. H. Blikra, S. Boyle, A. Braathen, J. Dehls, A. Elverhøi, B. Etzelmüller, S. Glimsdal, C. Harbitz, H. Heyerdahl, Ø. Høydal., H. Iwe, K. Karlsrud, S. Lacasse, I. Lecomte, C. Lindholm, O. Longva, F. Løvholt, F. Nadim, S. Nordal, B. Romstad, J. Røed and J. Strout, 2005, International Centre for Geohazards (ICG): Assessment, prevention and mitigation of geohazards: Norwegian Journal of Geology, v. 85, no. 1-2, p. 45–62.

Stoecklin, A., B. Friedli, and A. M. Puzrin, 2017, Sedimentation as a control for large submarine landslides: Mechanical modeling and analysis of the santa barbara basin: Journal of Geophysical Research: Solid Earth, v. 122, no. 11, p. 8645–8663, doi:10.1002/2017jb014752.

Sun, S., C. Hu, O. Garcia-Pineda, V. Kourafalou, M. Le Hénaff, and Y. Androulidakis, 2018, Remote sensing assessment of oil spills near a damaged platform in the Gulf of Mexico: Marine Pollution Bulletin, v. 136, p. 141-151, doi: 10.1016/j.marpolbul.2018.09.004.

Talling, P., M. Clare, M. Urlaub, E. Pope, J. Hunt, and S. Watt, 2014, Large submarine landslides on continental slopes: Geohazards, methane release, and climate change: Oceanography, v. 27, no. 2, p. 32–45, doi:10.5670/oceanog.2014.38.

Tappin, D. R., P. Watts, and S. T. Grilli, 2008, The Papua New Guinea tsunami of 17 July 1998: Anatomy of a catastrophic event: Natural Hazards and Earth System Sciences, v. 8, no. 2, p. 243–266, doi:10.5194/nhess-8-243-2008.

Underwood, M. B. and B. Dugan, 2021, Data report: Clay mineral assemblages within and beneath the Tuaheni landslide complex, IODP Expedition 372A site U1517, offshore New Zealand: Creeping Gas Hydrate Slides, doi:10.14379/iodp.proc.372a.201.2021.

Urlaub, M., J. Geersen, S. Krastel, and T. Schwenk, 2018, Diatom Ooze: Crucial for the generation of submarine mega-slides?: Geology, v. 46, no. 4, p. 331–334, doi:10.1130/g39892.1.

Urlaub, M., P. J. Talling, A. Zervos, and D. Masson, 2015, What causes large submarine landslides on low gradient (<2°) continental slopes with slow (~0.15 m/kyr) sediment accumulation?: Journal of Geophysical Research: Solid Earth, v. 120, no. 10, p. 6722–6739, doi:10.1002/2015jb012347.

Urlaub, M., P. J. Talling, and D. G. Masson, 2013, Timing and frequency of large submarine landslides: Implications for understanding triggers and future Geohazard: Quaternary Science Reviews, v. 72, p. 63–82, doi:10.1016/j.quascirev.2013.04.020.

APPENDIX A

SUPPLEMENTAL ELECTRONIC FILES

Unabridged raw and processed data is available for viewing and download in an online repository through Dr. Brandon Dugan. Included in this appendix are the consolidation and shear experiment data for each sample in an excel file denoted by experiment name. It also includes Matlab code for the sedimentation-fluid flow model available as a Matlab file.

Numerical Modeling Matlab Source Code File Name:

var_sed_flow_pstar_1d_1517_for_thesis_v3.m

This file includes the code and inputs to run the 1D sedimentation-fluid flow models. The code inputs such as permeability, sedimentation rates, initial porosity, etc. can be changed to fit specific values.

Processed DSS Experiment Data File Name**:**

Thesis_appendix_DSS_shear.xlsx

This file includes the shear strain, shear stress, shear induced pore pressure, and final consolidation vertical effective stress for each DSS experiment. The workbook denotes each experiment by the depth in mbsf of each experiment's sample. This data is useful in reproducing the shear strength values, the shear strength vs shear strain plots, and the shear induced pore pressure vs shear strain plots.